

Theory of correlated Chern insulators in twisted bilayer graphene

Xiaoyu Wang^{1,*} and Oskar Vafek^{1,2,†}

¹*National High Magnetic Field Lab, Tallahassee, FL 32310*

²*Department of Physics, Florida State University, Tallahassee, FL 32306*

Magic-angle twisted bilayer graphene is the best studied physical platform featuring moiré potential induced narrow bands with non-trivial topology and strong electronic correlations. Despite their significance, the Chern insulating states observed at a finite magnetic field—and extrapolating to a band filling, s , at zero field—remain poorly understood. Unraveling their nature is among the most important open problems in the province of moiré materials. Here we present the first comprehensive study of interacting electrons in finite magnetic field while varying the electron density, twist angle and heterostrain. Within a panoply of correlated Chern phases emerging at a range of twist angles, we uncover a unified description for the ubiquitous sequence of states with the Chern number t for $(s, t) = \pm(0, 4), \pm(1, 3), \pm(2, 2)$ and $\pm(3, 1)$. We also find correlated Chern insulators at unconventional sequences with $s + t \neq \pm 4$, as well as with fractional s , and elucidate their nature.

I. INTRODUCTION

The twisted bilayer graphene (TBG) has been a subject of intense theoretical and experimental investigation, in no small part due to its isolated, topologically non-trivial, narrow bands displaying rich correlated electron physics when partially occupied [1, 2]. As the twist angle between the two graphene layers is tuned toward the magic value of $\sim 1.05^\circ$ [3], TBG devices show a plethora of correlated phenomena including superconductivity, correlated insulating states and (quantized) anomalous Hall effect [4–26]. The non-trivial topology of the pair of narrow bands for a given valley and spin flavor is protected by the combined two-fold rotation symmetry about the out-of-plane axis C_{2z} (an emergent symmetry at low twist angle) and spinless time reversal symmetry T [27, 28]. The narrow band Hilbert space can thus be decomposed into a Chern +1 and a Chern –1 band [27, 29, 30]. One way to reveal the non-trivial topology of the narrow bands is to break C_{2z} via alignment with the hexagonal boron nitride substrate (hBN) and separate the Chern bands in energy. If in addition, the valley is spontaneously polarized, thus breaking T , the resulting state with one electron or hole per moiré unit cell becomes a Chern ± 1 insulator [31–34]. Indeed, experiments have observed anomalous Hall effect (AHE) near the filling of 3 electrons per moiré unit cell [10, 20] in hBN aligned samples. Further studies on non-aligned samples [21, 25] have also observed AHE near 1 electron per moiré unit cell. Theoretically, such zero-field Chern insulating states (zCIs) have been proposed to be energetically competitive near magic angle, when the Coulomb interaction exceeds the narrow bandwidth, even without the hBN alignment [30, 33, 35, 36].

An external magnetic field B , which preserves C_{2z} but breaks T , has been argued to be an alternative way to reveal the band topology [11, 19, 22], as evi-

denced by the experimental observations of correlated Chern insulating states (CCIs) with a finite Chern number t and extrapolating to a band filling s at $B = 0$ [6–8, 11, 13–16, 18, 19, 21–23, 25, 26]. Specifically, the most prominent sequence of CCIs has $(s, t) = (0, \pm 4), \pm(1, 3), \pm(2, 2), \pm(3, 1)$, consistent with selective population of the aforementioned $B = 0$ Chern ± 1 bands [11, 21, 22]. These experiments also report that some CCIs are stable at extremely low B , suggesting that they originate from the zCIs [11, 21].

However, CCIs are also observed in TBG devices away from the magic angle ($\sim 1.27^\circ$), where the bandwidth of the narrow bands is expected to be significantly larger than at 1.05° , without any observation of the correlated insulators at $B = 0$ [9]. Such CCIs appear only above a critical B , below which they transition into nearly compressible states for a fixed (s, t) . Similar phenomenology has also been reported in near-magic angle devices, leading to an alternative explanation of the CCIs invoking Stoner ferromagnetism within the magnetic subbands [7, 15, 16, 23], termed Hofstadter subband ferromagnets (HSFs) [15]. As argued theoretically [37–39], realistic heterostrain can also increase the bandwidth dramatically near the magic angle, likely placing many TBG devices in the intermediate coupling regime where the zCIs may not be energetically favored.

To date, the nature of these CCIs remains poorly understood. No microscopic calculation favoring either zCI or HSF has been carried out at $B \neq 0$, nor tying them to the relevant experiments. Moreover, the interplay of the CCIs with the competing states at $B = 0$ near the magic angle, such as the intervalley coherent states (IVCs) [29, 40], the incommensurate Kekulé spiral orders (IKSs) [38], and the striped and nematic states [14, 30, 41, 42], remains unclear.

Here we report the first comprehensive study of the interacting electrons within the TBG narrow bands directly at $B \neq 0$, and construct the phase diagram for a range of twist angles, B -fields and electron densities, with and without heterostrain. Consistent with the experimental observations, we find CCIs with $(0, \pm 4), \pm(1, 3), \pm(2, 2)$, and $\pm(3, 1)$, see Fig. 1 and Fig. S12. Such states

* xiaoyuw@magnet.fsu.edu

† vafek@magnet.fsu.edu

are found to be stabilized at higher B fields for twist angles as high as 1.38° (highest twist angle studied in this work), and for realistic heterostrain; based on analysis of their wavefunctions, we identify them as correlated Hofstadter ferromagnets (CHF). Similar to HSFs, they correspond to selective population of the valley and spin flavors, but of the interaction-renormalized magnetic subbands (see Fig. 2). Upon lowering B we find a first order phase transition into nearly compressible states at larger twist angles, or into incompressible states with intervalley coherence closer to the magic angle, at non-zero s . In the absence of heretostrain and at larger twist angles we similarly observe CHFs transitioning into nearly compressible states upon lowering B (see Fig. S12). As we lower the twist angle toward 1.05° , the incompressible $\pm(3, 1)$ state extends to lower B and crosses over into the finite B analog of the zCI, approaching maximal sublattice polarization. We refer to this state as the strong coupling Chern insulator (sCI). The $\pm(2, 2)$, $\pm(1, 3)$ and $(0, \pm 4)$ states also cross over into sCIs upon decreasing the twist angle, but they experience a first order phase transition into IVCs at low twist angles. The details of this transition depend sensitively on the model parameters, as shown in Fig. 3 and Fig. S20. Because there is no symmetry distinction between them, the CHF smoothly crosses over into the sCI as the twist angle is decreased toward the magic angle. In the phase diagram both with and without heterostrain, in addition to these prominent CCIs, we also find Quantum Hall ferromagnetic states (QHFM) emanating from band edges (Figs. S6, S14) and the charge neutrality point (Figs. S7, S15), CCIs with $s + t \neq \pm 4$, as well as fractional s that break the magnetic translation symmetry (Figs. 4, S9, S17).

II. MODEL AND METHOD:

We perform self-consistent Hartree-Fock analysis (B-SCHF) at $B \neq 0$ using the continuum Bistritzer-MacDonald (BM) Hamiltonian, with Coulomb interactions projected onto the narrow band Hilbert space. Here we briefly outline the formalism, additional details are in the Supplementary Information (SI). Starting with the (strained) BM Hamiltonian at rational magnetic flux ratios $\phi/\phi_0 = p/q$ where p and q are coprime integers, ϕ is the magnetic flux per moiré unit cell and $\phi_0 = h/e$ is the magnetic flux quantum, we solve for the Hofstadter spectra $\varepsilon_{\eta sr}(\mathbf{k})$ and associated eigenstates $|\Psi_{\eta sr}(\mathbf{k})\rangle$. Here $\eta = \mathbf{K}, \mathbf{K}'$ and $s = \uparrow, \downarrow$ are valley and spin quantum numbers, $r = 1, \dots, 2q$ is the magnetic subband index, and $\mathbf{k} = k_1 \mathbf{g}_1 + k_2 \mathbf{g}_2$ is the magnetic crystal momentum defined in the magnetic Brillouin zone with $k_1 \in [0, 1)$ and $k_2 \in [0, 1/q)$, and $\mathbf{g}_{i=1,2}$ are moiré reciprocal lattice vectors (see SI). Spin Zeeman splitting is also considered in this calculation. For the model parameters studied in this work, the gap to remote Hofstadter bands does not close at the magnetic fluxes of interest. We study interaction effects by projecting the screened Coulomb interaction

onto the narrow band Hilbert space. The Hamiltonian is given by:

$$H = \sum_{\eta sr, \mathbf{k}} \varepsilon_{\eta sr}(\mathbf{k}) d_{\eta sr, \mathbf{k}}^\dagger d_{\eta sr, \mathbf{k}} + \frac{1}{2A} \sum_{\mathbf{q}} V_{\mathbf{q}} \delta \hat{\rho}_{\mathbf{q}} \delta \hat{\rho}_{-\mathbf{q}}. \quad (1)$$

Here A is the total area of the system, $d_{\eta sr, \mathbf{k}}$ is the electron annihilation operator, $\delta \hat{\rho}_{\mathbf{q}}$ is the Fourier transform of the electron density operator projected onto the narrow bands, subtracting a background charge density [43–45]. It is given by:

$$\delta \hat{\rho}_{\mathbf{q}} = \sum_{\eta s, r r', \mathbf{k}, \mathbf{p}} \langle \Psi_{\eta sr}(\mathbf{k}) | e^{-i\mathbf{q}\cdot\mathbf{r}} | \Psi_{\eta sr'}(\mathbf{p}) \rangle \times \left(d_{\eta sr, \mathbf{k}}^\dagger d_{\eta sr', \mathbf{p}} - \frac{1}{2} \delta_{r, r'} \delta_{\mathbf{k}, \mathbf{p}} \right).$$

We consider a dual-gate screened Coulomb interaction of the form $V(\mathbf{q}) = \frac{2\pi e^2}{\epsilon_0 \epsilon_r |\mathbf{q}|} \tanh\left(\frac{|\mathbf{q}|\xi}{2}\right)$, with relative dielectric constant $\epsilon_r = 15$ and screening length $\xi = 4\sqrt{|\mathbf{L}_1||\mathbf{L}_2|}$, where $\mathbf{L}_{i=1,2}$ are the primitive moiré unit cell vectors (see SI). These parameters are chosen to match the overall change of chemical potential from empty to full occupation of the narrow bands in magic angle devices as extracted from the compressibility measurements as well as STM [6, 7, 46–48] (see also Fig. S2).

The B-SCHF calculation is carried out for a range of twist angles from 1.38° to 1.05° , both for unstrained model as well as for realistic uniaxial heterostrain strength of $\epsilon = 0.2\%$ and orientation $\varphi = 0^\circ$ (see SI for details). The respective non-interacting Hofstadter spectra and Wannier diagrams are shown in Fig. S1 and S11.

The projected Hamiltonian at $B \neq 0$ is invariant under the following set of symmetries [43, 49, 50]: C_{2z} , valley $U(1)_v$ and spin $U(1)_s$, many-body particle-hole P , magnetic translation symmetries generated by $\hat{t}_{\mathbf{L}_1}$ and $\hat{t}_{\mathbf{L}_2}$ (see SI). In the absence of heterostrain C_{3z} and $C_{2y}T$ also leave H invariant. P guarantees symmetry about the charge neutrality point, and therefore we present our results for the hole filling only.

III. RESULTS

We first address the finite B phase diagram for TBG subject to 0.2% of heterostrain. Fig. 1 gives an overview of the calculated single particle excitation gap Δ as a function of moiré unit cell filling (n/n_s) and magnetic flux ratio (ϕ/ϕ_0) for six twist angles 1.38° , 1.32° , 1.28° , 1.24° , 1.20° and 1.05° . The size of the gap is proportional to the radius of the solid circle. As seen, there is a rich panoply of correlated insulating states. We start by focusing on the sequence of CCIs with $(s, t) = (0, -4), (-1, -3), (-2, -2), (-3, -1)$, which are observed for all the twist angles studied, and marked in red in Fig. 1(c). At larger twist angles, CCIs along $(-3, -1), (-2, -2), (-1, -3)$ emerge at high ϕ/ϕ_0 , and

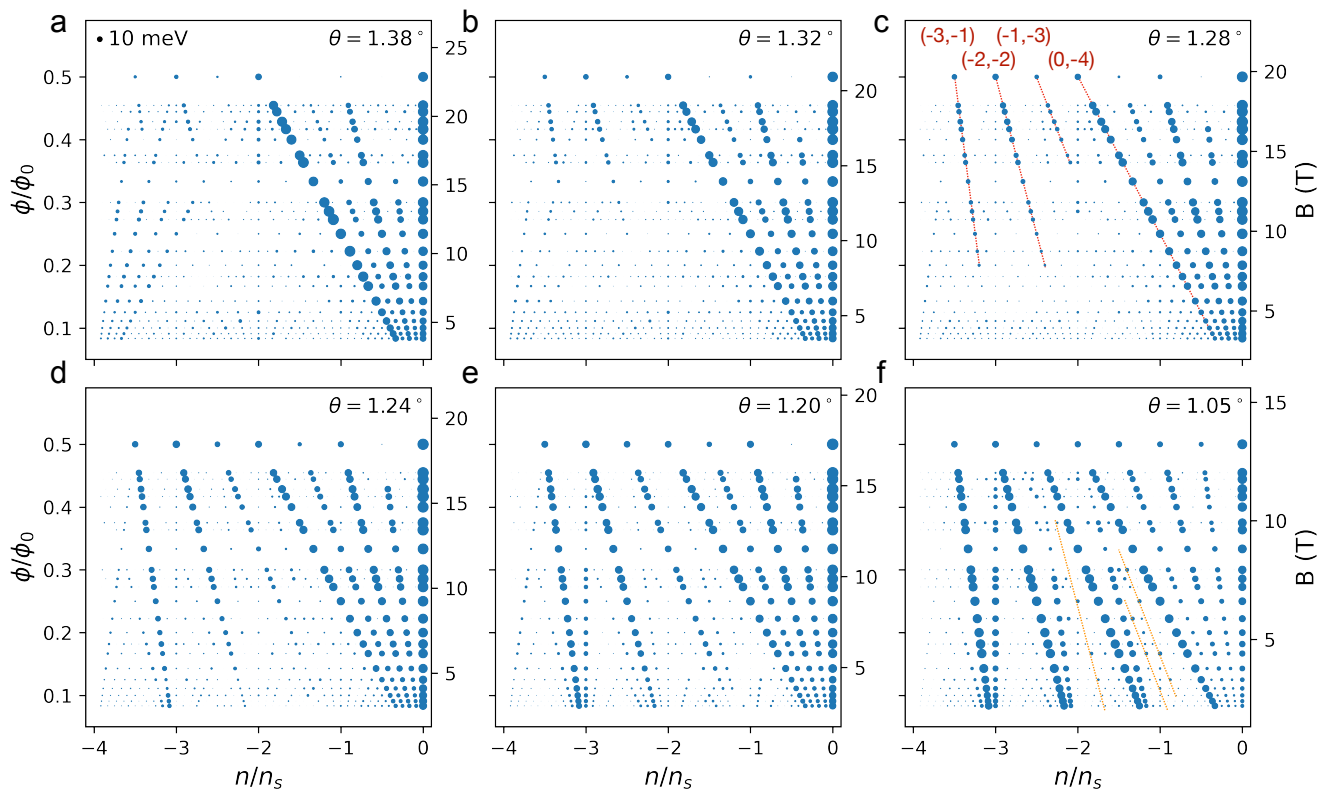


FIG. 1. Single-electron gap Δ as a function of electron filling and magnetic flux at twist angles 1.38° (a), 1.32° (b), 1.28° (c), 1.24° (d), 1.2° (e), and 1.05° (f). The size of the gaps are proportional to the radius of the respective solid circles, with the circle representation 10meV shown in (a). The sequence of $(s, t) = (0, -4), (-1, -3), (-2, -2),$ and $(-3, -1)$ are labeled by red dashed lines in (c). Chern insulating states with fractional s at $(s, t) = (-1/2, -3), (-2/3, -3),$ and $(-3/2, -2)$ are labeled by orange dashed lines in (f).

are replaced by nearly compressible states at lower ϕ/ϕ_0 via a first order phase transition. As the twist angle is lowered, they become more robust and can persist beyond the lowest flux ratio of 1/12 studied in this work.

To better understand their nature, we compile detailed results for two representative twist angles 1.38° [Figs. 2(a) to (f)] and 1.20° [Figs. 2(g) to (l)]. Fig. 2(a) shows the non-interacting spectra of valley \mathbf{K} and for one spin component (neglecting Zeeman effect) at $\theta = 1.32^\circ$. The magnetic subbands marked in red denote the Chern -1 group below the charge neutrality point. The analogous group of subbands above the charge neutrality point is related to it by particle hole symmetry, and also carries total Chern number -1 . The remaining two subbands emanate from the zeroth Landau levels (zLLs) of the energetically split Dirac points, and carry Chern number $+1$ each, such that the total Chern number of all magnetic subbands is zero. Fig. 2(b) shows the single-particle spectra including Coulomb interactions along $(s, t) = (-3, -1)$. At $\phi/\phi_0 \gtrsim 1/3$, the spectrum is gapped and the occupied states marked in red have a large overlap onto the states marked in red in Fig. 2(a). To quantify the overlap we make use of the Hartree-Fock density matrix, defined as $\hat{Q}_{\eta sr, \eta' s' r'}(\mathbf{k}) \equiv$

$\langle d_{\eta sr, \mathbf{k}}^\dagger d_{\eta' s' r', \mathbf{k}} \rangle$; for a state with unbroken valley $U(1)_v$ and spin $U(1)_s$ symmetries, it has the spin-valley diagonal form $\mathcal{Q}_{r, r'}^{(\eta s)}(\mathbf{k}) \delta_{\eta, \eta'} \delta_{s, s'}$. At high B , the $(-3, -1)$ CCI is valley and spin polarized. A representative $|\mathcal{Q}_{r, r'}^{\mathbf{K}\uparrow}(\mathbf{0})|$ is shown in Fig. 2(d). It is predominantly diagonal in the magnetic subband index, mostly occupying the lower $q - p$ magnetic subbands, i.e., the group states with total Chern -1 marked red in Fig. 2(a). At lower B , the gapped spectrum (red) in Fig. 2(b) transitions into a nearly gapless spectrum (green) via a first order phase transition. These low B states do not break the valley $U(1)_v$ and spin $U(1)_s$ symmetries, and their illustrative density matrix is shown in the Fig. 2(e). For $(-2, -2)$ and $(-1, -3)$ the density matrices of the CCIs at higher B are also shown in Fig. 2(d). These CCIs are also valley and spin polarized, similarly mostly populating the lower Chern -1 group of magnetic subbands for the specified valley and spin. $|\mathcal{Q}^{(\eta s)}(\mathbf{0})|$ are identical for all occupied flavors. As shown in Fig. 2(f), CCIs along $(-3, -1)$, $(-2, -2)$ and $(-1, -3)$ display quantitative differences in the critical B . In a recent transport experiment [17], the spin polarizations of the CCIs near the magic angle are identified, with $(-3, -1)$ and $(2, 2)$ being spin polarized,

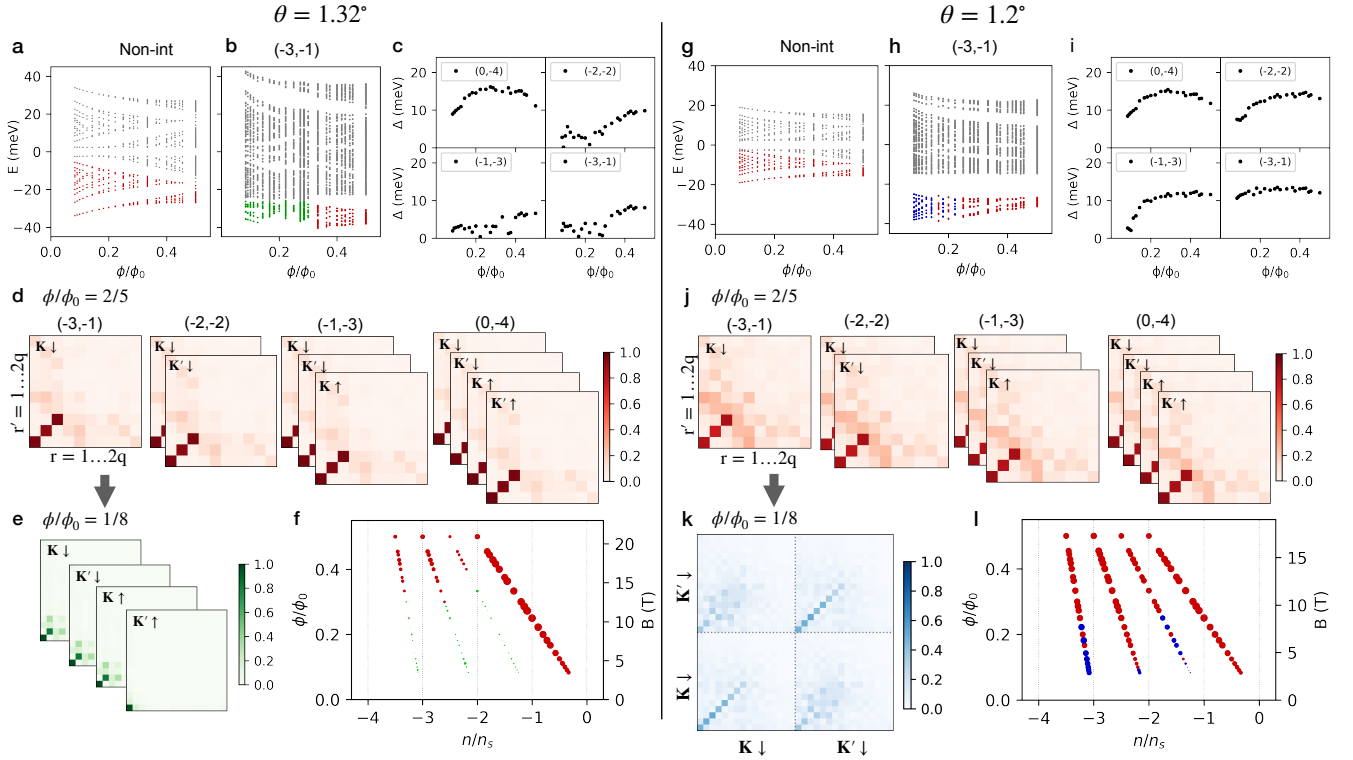


FIG. 2. Compilation of B-SCHF results at two representative twist angles, $\theta = 1.32^\circ$ (a-f) and $\theta = 1.2^\circ$ (g-l). The non-interacting spectra are shown in (a) and (g). The renormalized spectra along $(s, t) = (-3, -1)$ are shown in (b) and (h). The occupied electronic states are colored in red and green at 1.32° , signifying the first order phase transition between CHF's (red) and nearly compressible states (green). The occupied electronic states are colored in red and blue at 1.2° , signifying the first order phase transition between CHF's (red) and gapped states with intervalley coherence (blue). The alternating colors along $(-3, -1)$ and $(-1, -3)$ are due to near energetic degeneracies ($\sim 0.05\text{meV}$) between competing states (see Fig. S4), and are not resolved within our calculation. (c) and (i) show the non-monotonic behaviors of $\Delta(\phi/\phi_0)$ along $(s, t) = (0, -4)$, $(-1, -3)$, $(-2, -2)$, and $(-3, -1)$ Density matrix analysis. (d) and (j) show the absolute value of the non-vanishing matrix elements of the density matrices at $\phi/\phi_0 = 2/5$ at $\mathbf{k} = \mathbf{0}$. (e) and (k) are the absolute values of the representative density matrices at ϕ/ϕ_0 for a nearly compressible state (e) and an intervalley coherent state (k). (f) and (l) are replots of $\Delta(n/n_s, \phi/\phi_0)$, colored in the same manner as (b) and (h) respectively.

and $(-2, -2)$ being spin unpolarized. To better explain experiments, in particular the particle-hole asymmetry, microscopic modeling beyond the Bistritzer-MacDonald Hamiltonian is required [51], which is to be studied in future works.

Although these CCIs are closely related to the HSFs discussed in Ref. [7, 15, 23], the band structure renormalization is apparent in the non-vanishing off-diagonal matrix elements of $\mathcal{Q}_{r,r'}^{(\eta s)}(\mathbf{k})$, signifying hybridization with the higher energy subbands (marked by grey in Fig. 2(a)). For this reason we refer to them as CHF's. As further demonstrated in Fig. S3, the density matrices of the CHF's assume a much simpler structure when expressed in the eigenbasis of the valley and spin symmetric $(0, -4)$ Chern insulating state, which limits to an interaction-renormalized semimetal at $B = 0$ (see Fig. S2) [38]. Finally, in Fig. 2(c) we show the evolution of the single particle gap as a function of B along $(0, -4)$, $(-1, -3)$, $(-2, -2)$, and $(-3, -1)$. Generically, the gap shows a

broad plateau and non-monotonic dependence on B .

At the lower twist angle of $\theta = 1.2^\circ$ the CHF's at larger B are very similar to those at higher twist angles, however with stronger hybridization into the higher energy magnetic subbands, as seen in Fig. 2(j). In contrast to 1.32° , the CHF's lose via a first order phase transition to gapped states with intervalley coherence at lower B , as is apparent in the non-zero matrix elements $|\hat{Q}_{\mathbf{K}sr, \mathbf{K}'sr'}(\mathbf{0})|$ illustrated in Fig. 2(k). The intervalley coherent state may also break the magnetic translation symmetry $\hat{t}_{\mathbf{L}_2}$. However, our B-SCHF calculations cannot determine a unique wavevector \mathbf{q} associated with the translation symmetry breaking, suggesting that there is a manifold of $\mathbf{q} \neq 0$ intervalley coherent states with similar energies [38]. Interestingly, such intervalley coherent states hybridize subbands from the lower half of the (renormalized) Hofstadter spectra in each valley (see Fig. S5), similar to the IKS ground states at $B = 0$ discussed in Ref. [38].

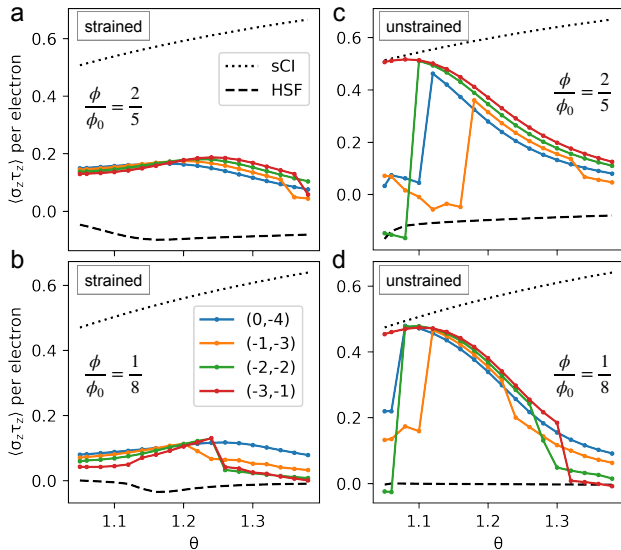


FIG. 3. Averaged $\sigma_z \tau_z$ per occupied single electron states at $(s, t) = (0, -4)$, $(-1, -3)$, $(-2, -2)$ and $(-3, -1)$ for (a) $\phi/\phi_0 = 2/5$ with heterostrain, (b) $\phi/\phi_0 = 1/8$ with heterostrain, (c) $\phi/\phi_0 = 2/5$ without heterostrain, and (d) $\phi/\phi_0 = 1/8$ without heterostrain. The dotted line in each panel is the value for sCI, and the dashed line corresponds to HSF.

A. Crossover to strong coupling regime

In order to clarify the connection between the CHF and the sCIs, we first note that the sCIs saturate the expectation value of $\sigma_z \tau_z$ for the occupied electronic states, where σ_z and τ_z are Pauli matrices acting in the sublattice and valley subspace respectively [29, 30, 43, 45]. The solid lines in Fig. 3(a) and (b) show calculated $\langle \sigma_z \tau_z \rangle$ per electron as a function of twist angle in the presence of heterostrain along $(0, -4)$, $(-1, -3)$, $(-2, -2)$, and $(-3, -1)$, for $\phi/\phi_0 = 2/5$ and $1/8$ respectively. For comparison, the upper dashed line corresponds to the sCI limit, and the lower dashed line to the HSF limit. This measure shows that the CHF are clearly distinct from both the HSFs and the sCIs in the presence of heterostrain. Qualitatively, the Coulomb repulsion favors an increased $\langle \sigma_z \tau_z \rangle$. The abrupt jump as angle is tuned (e.g., $\sim 1.5^\circ$ for $(-3, -1)$ in Fig. 3(b)) marks the first order transition between the aforementioned nearly compressible state and the CHF.

On the other hand, in the absence of heterostrain, as shown in Fig. 3(c) and (d), the CHF smoothly crosses over into the sCIs upon lowering the twist angle. For our model parameters, there is a collapse of the $\langle \sigma_z \tau_z \rangle$ at lower twist angles, when the CHF become energetically less favorable than populating the Landau quantized excitation spectra of the IVC states [33, 40, 45, 52]. As further demonstrated in Fig. S20, this transition depends sensitively on model parameters, and can be pushed toward lower ϕ/ϕ_0 (e.g., by moving toward the chiral limit,

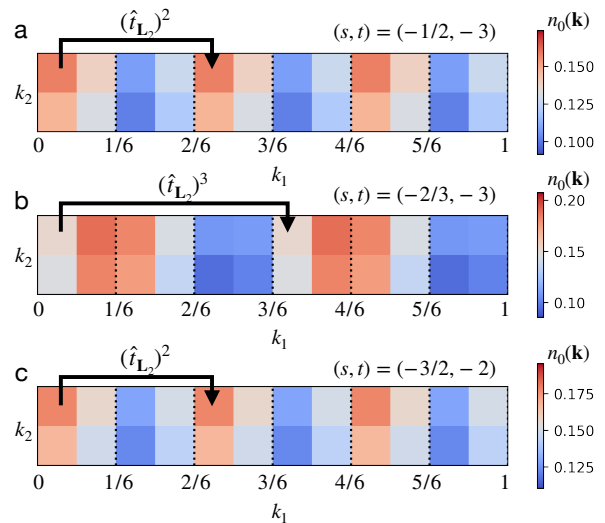


FIG. 4. Occupation number $n_0(\mathbf{k})$ of the lower zLL of the non-interacting spectra in valley \mathbf{K} and for spin \downarrow . Results are obtained at 1.05° for correlated Chern insulating states with fractional s , marked by the orange dashed lines in Fig. 1(f).

see SI and Ref. [53]). Refs. [11, 21] report that the $(2, 2)$ persist down to $\phi/\phi_0 \sim 1/100$, and therefore argue that they correspond to the zCIs (more precisely, sCIs). Our quantitative calculations clearly demonstrate that such states can indeed be stabilized at weak fields by small changes of the model parameters.

B. Additional CCIs

Besides the aforementioned CCIs, we also find additional correlated insulating states in the phase diagram with heterostrain (Fig. 1). The most prominent states emanate from the charge neutrality point ($n/n_s = 0$), and are identified as QHFs within the zLLs of the energetically split Dirac cones [54–56] (see Figs. S7). QHFs emanating from the band bottom ($n/n_s = -4$) are well developed at 1.38° but become progressively weaker as the angle decreases (see Figs. S6). Moreover, at higher ϕ/ϕ_0 a gapped state with $(s, t) = (-2, 0)$ is observed in Figs. 1(a-c). We identify it as a Quantum Spin Hall (QSH) insulator due to strong spin splitting near $\phi/\phi_0 = 1/2$, as demonstrated in the non-interacting Hofstadter spectra in Fig. S1 and the density matrices in Fig. S8.

Closer to the magic angle, we also find unusual sequences with $(s, t) = (-3, 0), (-2, -1), (-1, -2)$. These states have the same s as the sequence $(s, t) = (-3, -1), (-2, -2), (-1, -3)$ discussed previously, but with a Chern number that is higher by +1. They all have intervalley coherence, with structure of the density matrices resembling that of an IKS ground state. However, careful analysis shows that they do not correspond to populating the Landau quantized excitation spectra

of the CCIs along $(s, t) = (-3, -1), (-2, -2), (-1, -3)$. Rather, they are distinct intervalley coherent states with a reorganization of the intervalley coherence between the magnetic subbands (see Fig. S5).

At 1.05° , we also find CCIs with fractional s along $(-2/3, -3)$, $(-1/2, -3)$, and $(-3/2, -2)$, see Fig. 1(f). These states break magnetic translation symmetry. We identify them as striped states with period m along the \mathbf{L}_2 direction, such that the density matrix is invariant under $\hat{t}_{\mathbf{L}_2}^m$. Their respective density matrices are shown in Fig. S9. We use the electron occupation number of the lower zLL (see Fig. 2(a) and (i) for example) in valley \mathbf{K} and for spin \downarrow to illustrate the striped states. We define it as $n_0(\mathbf{k})$, and show its momentum dependence in the magnetic Brillouin zone at $\phi/\phi_0 = 1/6$ for $(-2/3, -3)$, $(-1/2, -3)$, and $(-3/2, -2)$ in Figs. 4 (a), (b) and (c) respectively. At $(-1/2, -3)$ and $(-3/2, 2)$, the fractional part of s corresponds to half-filling of a valley and spin flavor, and we identify the period of the striped state as $m = 2$. At $(-2/3, -3)$, the fractional part of s corresponds to two thirds filling of a flavor, and we identify the stripe period as $m = 3$.

IV. CONCLUSION

In summary, by performing a comprehensive self-consistent Hartree-Fock study of the continuum Bistritzer-MacDonald model in finite magnetic fields, we unravel the nature of the prominent correlated Chern insulators observed in a wide range of TBG experiments. For realistic heterostrain, these CCIs are stabilized at higher magnetic fields, and correspond to valley and spin polarizations of the interaction-renormalized magnetic subbands (CHF). Upon lowering magnetic

field, the CHF become energetically less favored, losing to nearly compressible states at larger twist angles and other gapped states with intervalley coherence at smaller twist angles. In absence of heterostrain and at higher magnetic fields, the CHF crosses over to the strong coupling Chern insulating states (sCIs) as the twist angle decreases. At lower fields, competing states with intervalley coherence become more energetically favored, and the transition is marked by a collapse of the averaged sublattice polarization per occupied single-electron state.

Our calculations also predict additional gapped correlated insulating states beyond the $(s, t) = (0, \pm 4), \pm(1, 3), \pm(2, 2), \pm(3, 1)$ sequence, notably the striped states at fractional s . Given that our calculations have direct access to the interaction renormalized single-electron excitation spectra at a given filling and magnetic field (see Fig. S10), comparisons with experiments such as STM can be made to facilitate the characterization of the panoply of correlated insulating states.

V. ACKNOWLEDGEMENTS

X.W. and O. V. acknowledge invaluable discussions with B. Andrei Bernevig, C. Lewandowski, J. Finney, M.-H. He and J. Kang. X.W. acknowledges financial support from the Gordon and Betty Moore Foundation's EPIQS Initiative Grant GBMF11070, National High Magnetic Field Laboratory through NSF Grant No. DMR-1157490 and the State of Florida. O.V. was supported by NSF Grant No. DMR-1916958 and is partially funded by the Gordon and Betty Moore Foundation's EPIQS Initiative Grant GBMF11070. Most of the computing for this project was performed on the HPC at the Research Computing Center at the Florida State University (FSU).

-
- [1] E. Y. Andrei and A. H. MacDonald, Graphene bilayers with a twist, *Nature Materials* **19**, 1265 (2020).
 - [2] L. Balents, C. R. Dean, D. K. Efetov, and A. F. Young, Superconductivity and strong correlations in moiré flat bands, *Nature Physics* **16**, 725 (2020).
 - [3] R. Bistritzer and A. H. MacDonald, Moiré bands in twisted double-layer graphene, *Proceedings of the National Academy of Sciences* **108**, 12233 (2011).
 - [4] Y. Cao, V. Fatemi, A. Demir, S. Fang, S. L. Tomarken, J. Y. Luo, J. D. Sanchez-Yamagishi, K. Watanabe, T. Taniguchi, E. Kaxiras, R. C. Ashoori, and P. Jarillo-Herrero, Correlated insulator behaviour at half-filling in magic-angle graphene superlattices, *Nature* **556**, 80 (2018).
 - [5] Y. Cao, V. Fatemi, S. Fang, K. Watanabe, T. Taniguchi, E. Kaxiras, and P. Jarillo-Herrero, Unconventional superconductivity in magic-angle graphene superlattices, *Nature* **556**, 43 (2018).
 - [6] S. L. Tomarken, Y. Cao, A. Demir, K. Watanabe, T. Taniguchi, P. Jarillo-Herrero, and R. C. Ashoori, Electronic compressibility of magic-angle graphene superlattices, *Phys. Rev. Lett.* **123**, 046601 (2019).
 - [7] J. M. Park, Y. Cao, K. Watanabe, T. Taniguchi, and P. Jarillo-Herrero, Flavour Hund's coupling, chern gaps and charge diffusivity in moiré graphene, *Nature* **592**, 43 (2021).
 - [8] Y. Xie, B. Lian, B. Jäck, X. Liu, C.-L. Chiu, K. Watanabe, T. Taniguchi, B. A. Bernevig, and A. Yazdani, Spectroscopic signatures of many-body correlations in magic-angle twisted bilayer graphene, *Nature* **572**, 101 (2019).
 - [9] M. Yankowitz, S. Chen, H. Polshyn, Y. Zhang, K. Watanabe, T. Taniguchi, D. Graf, A. F. Young, and C. R. Dean, Tuning superconductivity in twisted bilayer graphene, *Science* **363**, 1059 (2019).
 - [10] A. L. Sharpe, E. J. Fox, A. W. Barnard, J. Finney, K. Watanabe, T. Taniguchi, M. A. Kastner, and D. Goldhaber-Gordon, Emergent ferromagnetism near three-quarters filling in twisted bilayer graphene, *Science* **365**, 605 (2019).
 - [11] K. P. Nuckolls, M. Oh, D. Wong, B. Lian, K. Watanabe, T. Taniguchi, B. A. Bernevig, and A. Yazdani, Strongly correlated chern insulators in magic-angle twisted bilayer

- graphene, *Nature* **588**, 610 (2020).
- [12] K. P. Nuckolls, R. L. Lee, M. Oh, D. Wong, T. Soejima, J. P. Hong, D. Călugăru, J. Herzog-Arbeitman, B. A. Bernevig, K. Watanabe, T. Taniguchi, N. Regnault, M. P. Zaletel, and A. Yazdani, Quantum textures of the many-body wavefunctions in magic-angle graphene, *Nature* **620**, 525 (2023).
- [13] A. T. Pierce, Y. Xie, J. M. Park, E. Khalaf, S. H. Lee, Y. Cao, D. E. Parker, P. R. Forrester, S. Chen, K. Watanabe, T. Taniguchi, A. Vishwanath, P. Jarillo-Herrero, and A. Yacoby, Unconventional sequence of correlated chern insulators in magic-angle twisted bilayer graphene, *Nature Physics* **17**, 1210 (2021).
- [14] Y. Xie, A. T. Pierce, J. M. Park, D. E. Parker, E. Khalaf, P. Ledwith, Y. Cao, S. H. Lee, S. Chen, P. R. Forrester, K. Watanabe, T. Taniguchi, A. Vishwanath, P. Jarillo-Herrero, and A. Yacoby, Fractional chern insulators in magic-angle twisted bilayer graphene, *Nature* **600**, 439 (2021).
- [15] Y. Saito, J. Ge, L. Rademaker, K. Watanabe, T. Taniguchi, D. A. Abanin, and A. F. Young, Hofstadter subband ferromagnetism and symmetry-broken chern insulators in twisted bilayer graphene, *Nature Physics* **17**, 478 (2021).
- [16] J. Yu, B. A. Foutty, Z. Han, M. E. Barber, Y. Schattner, K. Watanabe, T. Taniguchi, P. Phillips, Z.-X. Shen, S. A. Kivelson, and B. E. Feldman, Correlated hofstadter spectrum and flavour phase diagram in magic-angle twisted bilayer graphene, *Nature Physics* **18**, 825 (2022).
- [17] J. C. Hoke, Y. Li, J. May-Mann, K. Watanabe, T. Taniguchi, B. Bradlyn, T. L. Hughes, and B. E. Feldman, Uncovering the spin ordering in magic-angle graphene via edge state equilibration (2023), [arXiv:2309.06583](https://arxiv.org/abs/2309.06583).
- [18] X. Lu, P. Stepanov, W. Yang, M. Xie, M. A. Aamir, I. Das, C. Urgell, K. Watanabe, T. Taniguchi, G. Zhang, A. Bachtold, A. H. MacDonald, and D. K. Efetov, Superconductors, orbital magnets and correlated states in magic-angle bilayer graphene, *Nature* **574**, 653 (2019).
- [19] I. Das, X. Lu, J. Herzog-Arbeitman, Z.-D. Song, K. Watanabe, T. Taniguchi, B. A. Bernevig, and D. K. Efetov, Symmetry-broken chern insulators and rashba-like landau-level crossings in magic-angle bilayer graphene, *Nature Physics* **17**, 710 (2021).
- [20] M. Serlin, C. L. Tschirhart, H. Polshyn, Y. Zhang, J. Zhu, K. Watanabe, T. Taniguchi, L. Balents, and A. F. Young, Intrinsic quantized anomalous hall effect in a moiré heterostructure, *Science* **367**, 900 (2020).
- [21] P. Stepanov, M. Xie, T. Taniguchi, K. Watanabe, X. Lu, A. H. MacDonald, B. A. Bernevig, and D. K. Efetov, Competing zero-field chern insulators in superconducting twisted bilayer graphene, *Phys. Rev. Lett.* **127**, 197701 (2021).
- [22] S. Wu, Z. Zhang, K. Watanabe, T. Taniguchi, and E. Y. Andrei, Chern insulators, van hove singularities and topological flat bands in magic-angle twisted bilayer graphene, *Nature Materials* **20**, 488 (2021).
- [23] Y. Choi, H. Kim, Y. Peng, A. Thomson, C. Lewandowski, R. Polski, Y. Zhang, H. S. Arora, K. Watanabe, T. Taniguchi, J. Alicea, and S. Nadj-Perge, Correlation-driven topological phases in magic-angle twisted bilayer graphene, *Nature* **589**, 536 (2021).
- [24] Y. Choi, H. Kim, C. Lewandowski, Y. Peng, A. Thomson, R. Polski, Y. Zhang, K. Watanabe, T. Taniguchi, J. Alicea, and S. Nadj-Perge, Interaction-driven band flattening and correlated phases in twisted bilayer graphene, *Nature Physics* **17**, 1375 (2021).
- [25] S. Grover, M. Bocarsly, A. Uri, P. Stepanov, G. Di Battista, I. Roy, J. Xiao, A. Y. Meltzer, Y. Myasoedov, K. Pareek, K. Watanabe, T. Taniguchi, B. Yan, A. Stern, E. Berg, D. K. Efetov, and E. Zeldov, Chern mosaic and berry-curvature magnetism in magic-angle graphene, *Nature Physics* **18**, 885 (2022).
- [26] A. Uri, S. Grover, Y. Cao, J. A. Crosse, K. Bagani, D. Rodan-Legrain, Y. Myasoedov, K. Watanabe, T. Taniguchi, P. Moon, M. Koshino, P. Jarillo-Herrero, and E. Zeldov, Mapping the twist-angle disorder and landau levels in magic-angle graphene, *Nature* **581**, 47 (2020).
- [27] H. C. Po, L. Zou, T. Senthil, and A. Vishwanath, Faithful tight-binding models and fragile topology of magic-angle bilayer graphene, *Phys. Rev. B* **99**, 195455 (2019).
- [28] Z. Song, Z. Wang, W. Shi, G. Li, C. Fang, and B. A. Bernevig, All magic angles in twisted bilayer graphene are topological, *Phys. Rev. Lett.* **123**, 036401 (2019).
- [29] N. Bultinck, E. Khalaf, S. Liu, S. Chatterjee, A. Vishwanath, and M. P. Zaletel, Ground state and hidden symmetry of magic-angle graphene at even integer filling, *Phys. Rev. X* **10**, 031034 (2020).
- [30] J. Kang and O. Vafek, Non-abelian dirac node braiding and near-degeneracy of correlated phases at odd integer filling in magic-angle twisted bilayer graphene, *Phys. Rev. B* **102**, 035161 (2020).
- [31] Y.-H. Zhang, D. Mao, and T. Senthil, Twisted bilayer graphene aligned with hexagonal boron nitride: Anomalous hall effect and a lattice model, *Phys. Rev. Res.* **1**, 033126 (2019).
- [32] N. Bultinck, S. Chatterjee, and M. P. Zaletel, Mechanism for anomalous hall ferromagnetism in twisted bilayer graphene, *Phys. Rev. Lett.* **124**, 166601 (2020).
- [33] B. Lian, Z.-D. Song, N. Regnault, D. K. Efetov, A. Yazdani, and B. A. Bernevig, Twisted bilayer graphene. iv. exact insulator ground states and phase diagram, *Phys. Rev. B* **103**, 205414 (2021).
- [34] J. Liu and X. Dai, Theories for the correlated insulating states and quantum anomalous hall effect phenomena in twisted bilayer graphene, *Phys. Rev. B* **103**, 035427 (2021).
- [35] M. Xie and A. H. MacDonald, Nature of the correlated insulator states in twisted bilayer graphene, *Phys. Rev. Lett.* **124**, 097601 (2020).
- [36] T. Soejima, D. E. Parker, N. Bultinck, J. Hauschild, and M. P. Zaletel, Efficient simulation of moiré materials using the density matrix renormalization group, *Phys. Rev. B* **102**, 205111 (2020).
- [37] Z. Bi, N. F. Q. Yuan, and L. Fu, Designing flat bands by strain, *Phys. Rev. B* **100**, 035448 (2019).
- [38] Y. H. Kwan, G. Wagner, T. Soejima, M. P. Zaletel, S. H. Simon, S. A. Parameswaran, and N. Bultinck, Kekulé spiral order at all nonzero integer fillings in twisted bilayer graphene, *Phys. Rev. X* **11**, 041063 (2021).
- [39] X. Wang, J. Finney, A. L. Sharpe, L. K. Rodenbach, C. L. Hsueh, K. Watanabe, T. Taniguchi, M. A. Kastner, O. Vafek, and D. Goldhaber-Gordon, Unusual magnetotransport in twisted bilayer graphene from strain-induced open fermi surfaces, *Proceedings of the National Academy of Sciences* **120**, e2307151120 (2023).

- [40] H. C. Po, L. Zou, A. Vishwanath, and T. Senthil, Origin of mott insulating behavior and superconductivity in twisted bilayer graphene, *Phys. Rev. X* **8**, 031089 (2018).
- [41] S. Liu, E. Khalaf, J. Y. Lee, and A. Vishwanath, Nematic topological semimetal and insulator in magic-angle bilayer graphene at charge neutrality, *Phys. Rev. Res.* **3**, 013033 (2021).
- [42] F. Xie, J. Kang, B. A. Bernevig, O. Vafek, and N. Regnault, Phase diagram of twisted bilayer graphene at filling factor $\nu = \pm 3$, *Phys. Rev. B* **107**, 075156 (2023).
- [43] B. A. Bernevig, Z.-D. Song, N. Regnault, and B. Lian, Twisted bilayer graphene. iii. interacting hamiltonian and exact symmetries, *Phys. Rev. B* **103**, 205413 (2021).
- [44] O. Vafek and J. Kang, Renormalization group study of hidden symmetry in twisted bilayer graphene with coulomb interactions, *Phys. Rev. Lett.* **125**, 257602 (2020).
- [45] X. Wang and O. Vafek, Narrow bands in magnetic field and strong-coupling hofstadter spectra, *Phys. Rev. B* **106**, L121111 (2022).
- [46] U. Zondiner, A. Rozen, D. Rodan-Legrain, Y. Cao, R. Queiroz, T. Taniguchi, K. Watanabe, Y. Oreg, F. von Oppen, A. Stern, E. Berg, P. Jarillo-Herrero, and S. Ilani, Cascade of phase transitions and dirac revivals in magic-angle graphene, *Nature* **582**, 203 (2020).
- [47] D. Wong, K. P. Nuckolls, M. Oh, B. Lian, Y. Xie, S. Jeon, K. Watanabe, T. Taniguchi, B. A. Bernevig, and A. Yazdani, Cascade of electronic transitions in magic-angle twisted bilayer graphene, *Nature* **582**, 198 (2020).
- [48] Y. Saito, F. Yang, J. Ge, X. Liu, T. Taniguchi, K. Watanabe, J. I. A. Li, E. Berg, and A. F. Young, Isospin pomeranchuk effect in twisted bilayer graphene, *Nature* **592**, 220 (2021).
- [49] K. Hejazi, C. Liu, H. Shapourian, X. Chen, and L. Balents, Multiple topological transitions in twisted bilayer graphene near the first magic angle, *Phys. Rev. B* **99**, 035111 (2019).
- [50] J. Herzog-Arbeitman, A. Chew, D. K. Efetov, and B. A. Bernevig, Reentrant correlated insulators in twisted bilayer graphene at 25 t (2π flux), *Phys. Rev. Lett.* **129**, 076401 (2022).
- [51] J. Kang and O. Vafek, Pseudomagnetic fields, particle-hole asymmetry, and microscopic effective continuum hamiltonians of twisted bilayer graphene, *Phys. Rev. B* **107**, 075408 (2023).
- [52] K. Singh, A. Chew, J. Herzog-Arbeitman, B. A. Bernevig, and O. Vafek, Topological heavy fermions in magnetic field (2023), [arXiv:2305.08171](https://arxiv.org/abs/2305.08171).
- [53] G. Tarnopolsky, A. J. Kruchkov, and A. Vishwanath, Origin of magic angles in twisted bilayer graphene, *Phys. Rev. Lett.* **122**, 106405 (2019).
- [54] K. Nomura and A. H. MacDonald, Quantum hall ferromagnetism in graphene, *Phys. Rev. Lett.* **96**, 256602 (2006).
- [55] M. Kharitonov, Phase diagram for the $\nu = 0$ quantum hall state in monolayer graphene, *Phys. Rev. B* **85**, 155439 (2012).
- [56] A. F. Young, C. R. Dean, L. Wang, H. Ren, P. Cadden-Zimansky, K. Watanabe, T. Taniguchi, J. Hone, K. L. Shepard, and P. Kim, Spin and valley quantum hall ferromagnetism in graphene, *Nature Physics* **8**, 550 (2012).

Supplemental Material for “Theory of correlated Chern insulators in twisted bilayer graphene”

I. TBG WITH HETEROSTRAIN AT ZERO MAGNETIC FIELD

We consider the limit of small twist angle θ and small deformations of moiré superlattice due to uniaxial heterostrain, such that the moiré reciprocal lattice vectors are given by: $\mathbf{g}_{i=1,2} = \mathcal{E}^T \mathbf{G}_{i=1,2}$ [37], where \mathbf{G}_i are reciprocal lattice vectors of the untwisted and undeformed monolayer graphene, and

$$\mathcal{E} = \mathcal{T}(\theta) + \mathcal{S}(\epsilon, \varphi), \quad (\text{S1})$$

where

$$\mathcal{T}(\theta) = \begin{pmatrix} 0 & -\theta \\ \theta & 0 \end{pmatrix}, \quad \mathcal{S}(\epsilon, \varphi) = R_\varphi^T \begin{pmatrix} -\epsilon & 0 \\ 0 & \nu\epsilon \end{pmatrix} R_\varphi. \quad (\text{S2})$$

Here $\{\epsilon, \varphi\}$ parameterize the uniaxial heterostrain strength and orientation, R_φ is the two-dimensional rotation matrix, and $\nu \approx 0.16$ is the Poisson ratio. The moiré lattice vectors $\mathbf{L}_{i=1,2}$ are uniquely defined through the relation $\mathbf{L}_i \cdot \mathbf{g}_j = 2\pi\delta_{ij}$. Specifically,

$$\mathbf{L}_1 = \frac{2\pi}{(\mathbf{g}_1 \times \mathbf{g}_2) \cdot \hat{z}} (\mathbf{g}_2 \times \hat{z}), \quad \mathbf{L}_2 = \frac{2\pi}{(\mathbf{g}_1 \times \mathbf{g}_2) \cdot \hat{z}} (\hat{z} \times \mathbf{g}_1). \quad (\text{S3})$$

We consider the strained Bistritzer-MacDonald (BM) Hamiltonian discussed in our recent work [39], with the continuum Hamiltonian given as:

$$H_\eta = \left(\sum_{l=t,b} H_{\eta,l}^{intra} \right) + H_\eta^{inter}, \quad (\text{S4})$$

where $\eta = \pm 1$ labels \mathbf{K} (\mathbf{K}') valleys of monolayer graphene, $l = t, b$ labels the top (bottom) of the two graphene layers. The interlayer Hamiltonian is given by:

$$H_\eta^{inter} \approx \int d^2\mathbf{r} \psi_{\eta,t}^\dagger(\mathbf{r}) \left(\sum_{j=1,2,3} T_{\eta,j} e^{-i\eta\mathbf{q}_j \cdot \mathbf{r}} \right) \psi_{\eta,b}(\mathbf{r}) + h.c., \quad (\text{S5})$$

where $\psi_{\eta,l}(\mathbf{r}) \equiv (\psi_{\eta,l,A}(\mathbf{r}), \psi_{\eta,l,B}(\mathbf{r}))^T$ is a spinor in the sublattice basis for a given valley and layer. We have suppressed the spin index for simplicity. $\mathbf{q}_{j=1,2,3}$ are the three nearest neighbor bonds of the reciprocal honeycomb lattice, and

$$T_{\eta,j} = w_0 \sigma_0 + w_1 \left(\cos \frac{2\pi(j-1)}{3} \sigma_x + \eta \sin \frac{2\pi(j-1)}{3} \sigma_y \right). \quad (\text{S6})$$

Here $(\sigma_0, \sigma_x, \sigma_y)$ are Pauli matrices acting on sublattice degrees of freedom. w_0 and w_1 are intra-sublattice and inter-sublattice tunneling strengths between the two layers. The “chiral limit” discussed in Ref. [53] corresponds to $w_0/w_1 = 0$.

The intra-layer Hamiltonian is given by:

$$H_{\eta,l}^{intra} = \alpha \int d^2\mathbf{r} \psi_{\eta,l}^\dagger(\mathbf{r}) (\text{tr}[\mathcal{E}_l] \sigma_0) \psi_{\eta,l}(\mathbf{r}) + \frac{\hbar v_F}{a} \int d^2\mathbf{r} \psi_{\eta,l}^\dagger(\mathbf{r}) [(-i\nabla - \mathbf{A}_{\eta,l}) \cdot (\eta\sigma_x, \sigma_y)] \psi_{\eta,l}(\mathbf{r}), \quad (\text{S7})$$

where the first term is the deformation potential that couples to the electron density. $\mathbf{A}_{\eta,l}$ is the pseudovector potential that comes from changes in the inter-sublattice hopping due to deformations, and changes sign between graphene valleys. It is given as $\mathbf{A}_{\eta,l} = \frac{\sqrt{3}\beta}{2a} \eta (\epsilon_{l,xx} - \epsilon_{l,yy}, -2\epsilon_{l,xy})$.

We use $\alpha \approx -4.1$ eV and $\beta \approx 3.14$. We further fix $\hbar v_F/a = 2.68$ eV, $w_1 = 110$ meV and $w_0/w_1 = 0.7$ in our calculations, and also set constants $\hbar = a = 1$ in the remainder of this document. Other values of w_0/w_1 are also used and discussed in the manuscript as a way to stabilize the strong-coupling Chern insulating states.

II. TBG IN MAGNETIC FIELD

A. Landau level wavefunctions of monolayer graphene

We begin with a brief discussion of the Landau level (LL) eigenstates of the Dirac Hamiltonian of monolayer graphene. In a finite magnetic field B , the Dirac Hamiltonian in valleys \mathbf{K} and \mathbf{K}' are given by (here for negative charged electrons, the minimal coupling is $\mathbf{p} + e\mathbf{A}$ where e is positive):

$$\hat{H}_l^{\mathbf{K}}(\mathbf{p} + e\mathbf{A}) = v_F \vec{\sigma} \cdot (\mathbf{p} - \mathbf{K}_l + e\mathbf{A}), \quad (\text{S8})$$

$$\hat{H}_l^{\mathbf{K}'}(\mathbf{p} + e\mathbf{A}) = -v_F \vec{\sigma}^* \cdot (\mathbf{p} - \mathbf{K}'_l + e\mathbf{A}). \quad (\text{S9})$$

Here $l = 1, 2$ is the layer index, $\mathbf{K}_l = (K_{l,x}, K_{l,y})$ is the position of the Dirac cone in the reciprocal space.

We choose the Landau gauge such that the vector potential $\mathbf{A} \equiv Bx\hat{y}$, where the global $x - y$ coordinate system is defined such that \mathbf{L}_2 is along the $+\hat{y}$ direction. When TBG is subject to heterstrain, this amounts to a small angle rotation θ_0 of the global coordinate system with respect to the case in absence of heterostrain. The eigenstates of the Dirac Hamiltonian are solved by going to the harmonic oscillator basis: $x = \frac{\ell}{\sqrt{2}}(a + a^\dagger)$, and $p_x = \frac{1}{i\sqrt{2}\ell}(a - a^\dagger)$, where $\ell \equiv 1/\sqrt{eB}$ is the magnetic length.

In valley \mathbf{K} , the particle-hole symmetric LL eigenstates are given as:

$$\langle \mathbf{r} | \psi_{n\gamma l}(k_2) \rangle = e^{iK_{l,x}x} e^{i\frac{2\pi}{L_2}k_2y} \frac{1}{\sqrt{2}} \begin{pmatrix} -i\gamma e^{-i\theta_0} \phi_{n-1}(x + \tilde{k}_{2,l}\ell^2) \\ \phi_n(x + \tilde{k}_{2,l}\ell^2) \end{pmatrix}, \quad (\text{S10})$$

where $\epsilon_{n\gamma} = \frac{v_F}{\ell} \gamma \sqrt{2n}$ is the energy of the Dirac Hamiltonian, labeled by $n = 1, 2, \dots$, and $\gamma = \pm 1$ corresponds to positive and negative energy solutions. We have defined $L_2 \equiv |\mathbf{L}_2|$. In addition, there is an anomalous zero energy state given by

$$\langle \mathbf{r} | \psi_{0l}(k_2) \rangle = e^{iK_{l,x}x} e^{i\frac{2\pi}{L_2}k_2y} \begin{pmatrix} 0 \\ \phi_0(x + \tilde{k}_{2,l}\ell^2) \end{pmatrix} \quad (\text{S11})$$

which lives on the B sublattice. $\phi_n(x)$ is the eigenfunction of $a^\dagger a$, and is given to be:

$$\phi_n(x) = \frac{1}{\pi^{1/4}} \frac{1}{\sqrt{2^n n!}} e^{-x^2/2\ell^2} H_n(x/\ell), \quad (\text{S12})$$

where $H_n(x)$ is the Hermite polynomial. The shift in the position for a given wavevector $k_2 \mathbf{g}_2$ is given by:

$$\tilde{k}_{2,l}\ell^2 = \left(\frac{2\pi}{L_2} k_2 - K_{l,y} \right) \ell^2. \quad (\text{S13})$$

In valley \mathbf{K}' , the Landau level wavefunctions are solved in a similar manner, and the LL eigenbasis is given by:

$$\langle \mathbf{r} | \psi_{n\gamma l}(k_2) \rangle = e^{iK'_{l,x}x} e^{i\frac{2\pi}{L_2}k_2y} \frac{1}{\sqrt{2}} \begin{pmatrix} \phi_n(x + \tilde{k}_{2,l}\ell^2) \\ i\gamma e^{-i\theta_0} \phi_{n-1}(x + \tilde{k}_{2,l}\ell^2) \end{pmatrix} \quad (\text{S14})$$

with eigenenergy $\epsilon_{n\gamma} = v_F \gamma \frac{\sqrt{2n}}{\ell}$, and eigenstate for the zeroth LL:

$$\langle \mathbf{r} | \psi_{0l}(k_2) \rangle = e^{iK'_{l,x}x} e^{i\frac{2\pi}{L_2}k_2y} \begin{pmatrix} \phi_0(x + \tilde{k}_{2,l}\ell^2) \\ 0 \end{pmatrix}. \quad (\text{S15})$$

For notational convenience we define a ket state $|\Phi_{n\gamma l}^{(\eta)}(k_2)\rangle$ such that:

$$\langle \mathbf{r} | \psi_{n\gamma l}^{(\eta)}(k_2) \rangle = e^{iK_{\eta l,x}x} e^{i\frac{2\pi}{L_2}k_2y} \langle \mathbf{r} | \Phi_{n\gamma l}^{(\eta)}(k_2) \rangle. \quad (\text{S16})$$

The ket state has the following real space properties:

$$\langle \mathbf{r} | \Phi_{n\gamma l}^{(\eta)}(k_2) \rangle \equiv \Phi_{n\gamma l}^{(\eta)}(x + \tilde{k}_{2,l}\ell^2), \quad (\text{S17})$$

where the definitions of $\Phi_{n\gamma l}^{(\eta)}(x + \tilde{k}_{2,l}\ell^2)$ are inferred from Eqs. (S10), (S11), (S14) and (S15).

B. Magnetic translation group eigenstates

At rational magnetic flux ratios $\phi/\phi_0 = p/q$ where $\phi_0 = h/e$ is the magnetic flux quantum, p and q are coprime integers, the strained BM Hamiltonian is invariant under magnetic translations, $\hat{t}_{\mathbf{L}_1}$ and $\hat{t}_{\mathbf{L}_2}$, such that:

$$\hat{t}_{\mathbf{L}_1} = e^{-i\mathbf{q}\phi\cdot(\mathbf{r}-\mathbf{L}_1/2)}\hat{T}_{\mathbf{L}_1}, \quad \hat{t}_{\mathbf{L}_2} = \hat{T}_{\mathbf{L}_2}, \quad \mathbf{q}\phi = \frac{2\pi}{|\mathbf{L}_2|}\frac{\phi}{\phi_0}\hat{y}, \quad \hat{t}_{\mathbf{L}_2}\hat{t}_{\mathbf{L}_1} = e^{i2\pi\phi/\phi_0}\hat{t}_{\mathbf{L}_1}\hat{t}_{\mathbf{L}_2}. \quad (\text{S18})$$

Here $\hat{T}_{\mathbf{L}_i}\psi(\mathbf{r}) = \psi(\mathbf{r} - \mathbf{L}_i)$. As a result, the eigenstates of the strained Bistritzer-MacDonald Hamiltonian are simultaneous eigenstates of the magnetic translation group (MTG). The MTG basis states can be generated from the LL basis states discussed in the previous section:

$$\begin{aligned} |V_{n\gamma l}^{(\eta)}(\mathbf{k})\rangle &= \frac{1}{\sqrt{\mathcal{N}}} \sum_{s_1=-\infty}^{\infty} e^{i2\pi k_1 s_1} \hat{t}_{\mathbf{L}_1}^{s_1} |\psi_{n\gamma l}^{(\eta)}(k_2)\rangle \\ &= \frac{1}{\sqrt{\mathcal{N}}} \sum_{s_1} e^{i2\pi(k_1 - k_2 \frac{L_{1y}}{L_2})s_1} e^{i\frac{1}{2}s_1^2 \mathbf{q}\phi\cdot\mathbf{L}_1} e^{-is_1 K_{\eta l, x} L_{1, x}} \left| \psi_{n\gamma l}^{(\eta)}\left(k_2 - s_1 \frac{\phi}{\phi_0}\right) \right\rangle, \end{aligned} \quad (\text{S19})$$

where \mathcal{N} is a normalization factor, and $\mathbf{k} \equiv k_1 \mathbf{g}_1 + k_2 \mathbf{g}_2$. It is straightforward to check that:

$$|V_{n\gamma l}^{(\eta)}(k_1 + 1, k_2)\rangle = |V_{n\gamma l}^{(\eta)}(k_1, k_2)\rangle, \quad (\text{S20})$$

$$\left| V_{n\gamma l}^{(\eta)}\left(k_1, k_2 + \frac{\phi}{\phi_0}\right) \right\rangle = e^{iK_{l, x} L_{1, x}} e^{-i2\pi(k_1 - k_2 \frac{L_{1y}}{L_2})} |V_{n\gamma l}^{(\eta)}(k_1, k_2)\rangle, \quad (\text{S21})$$

$$\hat{t}_{\mathbf{L}_2} |V_{n\gamma l}^{(\eta)}(k_1, k_2)\rangle = e^{-i2\pi k_2} \left| V_{n\gamma l}^{(\eta)}\left(k_1 + \frac{\phi}{\phi_0}, k_2\right) \right\rangle, \quad (\text{S22})$$

$$\langle V_{n\gamma l}^{(\eta)}(k_1, k_2) | V_{n'\gamma' l'}^{(\eta')}(p_1, p_2) \rangle = \delta_{\eta, \eta'} \delta_{l, l'} \delta_{k_1, k_2} \delta_{p_1, p_2} \delta_{n, n'} \delta_{\gamma, \gamma'}. \quad (\text{S23})$$

Therefore, the MTG eigenstates defined in $(k_1, k_2) \in [0, 1) \times [0, \frac{\phi}{\phi_0})$ form a complete and orthonormal basis set in a finite magnetic field. This is referred to as the magnetic Brillouin zone. In order to find the eigenstates of the narrow bands for strained BM Hamiltonian in B , we also need to compute the matrix elements of the interlayer tunneling terms in the above MTG basis states. From now on we work with rational flux ratio $\phi/\phi_0 = p/q$, where p and q are coprime.

C. Matrix elements for a generic operator $A_{\mathbf{q}} \equiv \hat{A}e^{-i\mathbf{q}\cdot\mathbf{r}}$

We first work out the matrix elements for a generic operator in the MTG eigenstates, $A_{\mathbf{q}} = \hat{A}e^{-i\mathbf{q}\cdot\mathbf{r}}$, where \hat{A} is a space-independent matrix in the layer, sublattice, and valley basis. For example, the Fourier transform of the electron density operator, $\hat{\rho}_{\mathbf{q}} \equiv \hat{\rho}e^{-i\mathbf{q}\cdot\mathbf{r}}$, has $\hat{\rho} = \hat{I}$, where \hat{I} is the identity matrix. We denote $\mathbf{q} = q_1 \mathbf{g}_1 + q_2 \mathbf{g}_2$ and $\mathbf{p} = p_1 \mathbf{g}_1 + p_2 \mathbf{g}_2$. We therefore have:

$$\begin{aligned} &\langle V_{n\gamma l}^{(\eta)}(\mathbf{k}) | A_{\mathbf{q}} | V_{n'\gamma' l'}^{(\eta')}(\mathbf{p}) \rangle \\ &= \frac{1}{\mathcal{N}} \sum_{s_1, s'_1} e^{-i2\pi k_1 s_1} e^{i2\pi p_1 s'_1} \langle \psi_{n\gamma l}^{(\eta)}(k_2) | \hat{t}_{\mathbf{L}_1}^{-s_1} \hat{A} e^{-i\mathbf{q}\cdot\mathbf{r}} \hat{t}_{\mathbf{L}_1}^{s'_1} | \psi_{n'\gamma' l'}^{(\eta')}(p_2) \rangle \\ &= \frac{1}{\mathcal{N}} \sum_{s_1, s'_1} e^{-i2\pi(k_1 + q_1)s_1} e^{i2\pi p_1 s'_1} \langle \psi_{n\gamma l}^{(\eta)}(k_2) | \hat{A} e^{-i\mathbf{q}\cdot\mathbf{r}} \hat{t}_{\mathbf{L}_1}^{s'_1 - s_1} | \psi_{n'\gamma' l'}^{(\eta')}(p_2) \rangle \\ &= \delta_{[p_1 - k_1 - q_1]_1, 0} \sum_s e^{i2\pi p_1 s} \langle \psi_{n\gamma l}^{(\eta)}(k_2) | \hat{A} e^{-i\mathbf{q}\cdot\mathbf{r}} \hat{t}_{\mathbf{L}_1}^{s_1} | \psi_{n'\gamma' l'}^{(\eta')}(p_2) \rangle \\ &= \delta_{[p_1 - k_1 - q_1]_1, 0} \sum_s e^{i2\pi(p_1 - p_2 \frac{L_{1y}}{L_2})s} e^{\frac{i}{2}s^2 \mathbf{q}\phi\cdot\mathbf{L}_1} e^{-is K_{\eta' l', x} L_{1, x}} \langle \psi_{n\gamma l}^{(\eta)}(k_2) | \hat{A} e^{-i\mathbf{q}\cdot\mathbf{r}} \left| \psi_{n'\gamma' l'}^{(\eta')}\left(p_2 - \frac{sp}{q}\right) \right\rangle \\ &= \delta_{[p_1 - k_1 - q_1]_1, 0} \sum_s \delta_{p_2 - sp/q, k_2 + q_2} e^{i2\pi(p_1 - p_2 \frac{L_{1y}}{L_2})s} e^{\frac{i}{2}s^2 \mathbf{q}\phi\cdot\mathbf{L}_1} e^{-is K_{\eta' l', x} L_{1, x}} \langle \Phi_{n\gamma l}^{(\eta)}(k_2) | \hat{A} e^{-i\tilde{q}\cdot x} \left| \Phi_{n'\gamma' l'}^{(\eta')}(k_2 + q_2) \right\rangle \\ &\equiv \delta_{[p_1 - k_1 - q_1]_1, 0} \sum_s \delta_{p_2 - sp/q, k_2 + q_2} e^{i2\pi(p_1 - p_2 \frac{L_{1y}}{L_2})s} e^{\frac{i}{2}s^2 \mathbf{q}\phi\cdot\mathbf{L}_1} e^{-is K_{\eta' l', x} L_{1, x}} \mathcal{A}_{n\gamma l, n'\gamma' l'}^{\eta\eta'}(k_2, k_2 + q_2). \end{aligned} \quad (\text{S24})$$

The notation $[b]_a$ represents b modulo a , with $a > 0$. We have defined:

$$\tilde{q}_x \equiv q_x + K_{\eta l, x} - K_{\eta' l', x}. \quad (\text{S25})$$

We proceed to work out the 1D integration by noting that:

$$\left\langle x \left| \Phi_{n\gamma l}^{(\eta)}(k_2) \right\rangle = \Phi_{n\gamma l}^{(\eta)}(x + \tilde{k}_{2, \eta l} \ell^2) = e^{ip_x \tilde{k}_{2, \eta l} \ell^2} \Phi_{n\gamma l}^{(\eta)}(x) \equiv \hat{T}_x(\tilde{k}_{2, \eta l} \ell^2) \Phi_{n\gamma l}^{(\eta)}(x), \quad (\text{S26})$$

and as a result:

$$\begin{aligned} \mathcal{A}_{n\gamma l, n'\gamma' l'}^{\eta\eta'}(k_2, k_2 + q_2) &= \left\langle \Phi_{n\gamma l}^{(\eta)}(0) \left| \hat{T}_x(-\tilde{k}_{2, \eta l} \ell^2) \hat{A} e^{-i\tilde{q}_x x} \hat{T}_x(\widetilde{(k+q)}_{2, \eta' l'} \ell^2) \right| \Phi_{n'\gamma' l'}^{(\eta')}(0) \right\rangle \\ &= e^{i\tilde{q}_x \tilde{k}_{2, \eta l} \ell^2} \left\langle \Phi_{n\gamma l}^{(\eta)}(0) \left| \hat{A} e^{-i\tilde{q}_x x} e^{i\tilde{q}_y \ell^2 p_x} \right| \Phi_{n'\gamma' l'}^{(\eta')}(0) \right\rangle \\ &= e^{i\tilde{q}_x \tilde{k}_{2, \eta l} \ell^2} e^{\frac{i}{2} \tilde{q}_x \tilde{q}_y \ell^2} \left\langle \Phi_{n\gamma l}^{(\eta)}(0) \left| \hat{A} e^{c-a+c+a^\dagger} \right| \Phi_{n'\gamma' l'}^{(\eta')}(0) \right\rangle \\ &\equiv e^{i\tilde{q}_x \tilde{k}_{2, \eta l} \ell^2} e^{\frac{i}{2} \tilde{q}_x \tilde{q}_y \ell^2} \hat{\mathcal{A}}_{n\gamma l, n'\gamma' l'}^{\eta\eta'}, \end{aligned} \quad (\text{S27})$$

where $\hat{\mathcal{A}}_{n\gamma l, n'\gamma' l'}^{\eta\eta'}$ can be expressed in terms of associated Laguerre polynomials [45], and:

$$\tilde{q}_y \equiv q_y + K_{\eta l, y} - K_{\eta' l', y}, \quad c_{\pm} = -i \frac{\ell}{\sqrt{2}} (\tilde{q}_x \mp i\tilde{q}_y). \quad (\text{S28})$$

Next we consider the implications of the δ function constraints. Firstly we have:

$$q_1 = p_1 - k_1 + r, \quad r \in \mathbb{Z}. \quad (\text{S29})$$

Secondly we have:

$$q_2 = p_2 - k_2 - \frac{sp}{q}, \quad s \in \mathbb{Z}. \quad (\text{S30})$$

This shows that above matrix elements are non-vanishing only if:

$$\mathbf{q} \equiv \mathbf{p} - \mathbf{k} + r\mathbf{g}_1 - \frac{sp}{q}\mathbf{g}_2, \quad r, s \in \mathbb{Z}. \quad (\text{S31})$$

Finally, we have the following expression for the matrix elements:

$$\begin{aligned} &\left\langle V_{n\gamma l}^{(\eta)}(\mathbf{k}) \left| A_{\mathbf{q}} \right| V_{n'\gamma' l'}^{(\eta')}(\mathbf{p}) \right\rangle \\ &= \delta_{[p_1 - k_1 - q_1]_1, 0} \sum_s \delta_{p_2 - sp/q, k_2 + q_2} e^{i2\pi(p_1 - p_2 - \frac{L_{1y}}{L_2})s} e^{i\frac{s}{2} \mathbf{q} \cdot \mathbf{L}_1} e^{-isK_{\eta' l', x} L_{1, x}} e^{i\tilde{q}_x \tilde{k}_{2, \eta l} \ell^2} e^{\frac{i}{2} \tilde{q}_x \tilde{q}_y \ell^2} \hat{\mathcal{A}}_{n\gamma l, n'\gamma' l'}^{\eta\eta'}. \end{aligned}$$

with $\tilde{\mathbf{q}} \equiv \mathbf{q} + \mathbf{K}_{\eta l} - \mathbf{K}_{\eta' l'}$.

D. Matrix elements of strained BM Hamiltonian

1. Interlayer terms

The interlayer terms are a special case of the generic $A_{\mathbf{q}}$ discussed in the previous section. For bottom to top layer tunneling we have (see Eq. (S24)):

$$\begin{aligned} &\left\langle V_{n\gamma b}^{(\eta)}(\mathbf{k}) \left| T_{\eta, j} e^{-i\eta \mathbf{q}_j \cdot \mathbf{r}} \right| V_{n'\gamma' t}^{(\eta')}(\mathbf{p}) \right\rangle \\ &= \delta_{\eta\eta'} \delta_{[p_1 - k_1 - q_1]_1, 0} \sum_s \delta_{p_2 - sp/q, k_2 + q_2} e^{i2\pi(p_1 - p_2 - \frac{L_{1y}}{L_2})s} e^{i\frac{s}{2} \mathbf{q} \cdot \mathbf{L}_1} e^{-isK_{\eta t, x} L_{1, x}} e^{i\tilde{q}_x \tilde{k}_{2, \eta l} \ell^2} e^{\frac{i}{2} \tilde{q}_x \tilde{q}_y \ell^2} \hat{\mathcal{T}}_{n\gamma b, n'\gamma' t}^{(\eta, j)}, \end{aligned} \quad (\text{S32})$$

where $\mathbf{q}_j = \mathbf{0}, \mathbf{g}_2, \mathbf{g}_1 + \mathbf{g}_2$. For notational convenience we have also defined $\mathbf{q}_j \equiv q_1 \mathbf{g}_1 + q_2 \mathbf{g}_2$ where $q_{1,2}$ are integers (with implicit dependence on j). Plugging these into the δ -function constraints we have:

$$p_1 = k_1, \quad p_2 - k_2 - \frac{sp}{q} \in \mathbb{Z}. \quad (\text{S33})$$

We can split the momentum p_2, k_2 into strips of $[0, 1/q), \dots, [(p-1)/q, p/q)$, by redefining:

$$p_2 \rightarrow p_2 + r'_2/q, \quad k_2 \rightarrow k_2 + r_2/q, \quad k_2, p_2 \in [0, 1/q). \quad (\text{S34})$$

It is clear then that $(k_1, k_2) \in [0, 1) \times [0, 1/q)$ are good quantum numbers under moire periodic potential, and that:

$$r'_2 = r_2 + qq_2 + sp \Rightarrow r_2 = [r_2 + qq_2]_p, \quad s = -(r_2 + qq_2)/p. \quad (\text{S35})$$

2. Narrow band eigenstates

From above analysis, it is clear that the narrow band eigenstates in the Landau gauge are labeled by $(k_1, k_2) \in [0, 1) \times [0, 1/q)$, and an additional $2q$ quantum numbers per valley and spin. Generally we can denote them as:

$$\left| \Psi_a^{(\eta)}(\mathbf{k}) \right\rangle \equiv \sum_{n\gamma l} \sum_{r_2=0}^{p-1} U_{n\gamma l r_2, a}^{(\eta)}(\mathbf{k}) \left| V_{n\gamma l}^{(\eta)}(k_1, k_2 + r_2/q) \right\rangle, \quad a = 1, \dots, 2q. \quad (\text{S36})$$

3. Degeneracy of magnetic subbands generated by $\hat{t}_{\mathbf{L}_2}$

The non-interacting Hamiltonian $H_{\text{non-int}}$ in valley η acting on the narrow band eigenstates is:

$$H_{\text{non-int}} \left| \Psi_a^{(\eta)}(\mathbf{k}) \right\rangle = \varepsilon_a^{(\eta)}(\mathbf{k}) \left| \Psi_a^{(\eta)}(\mathbf{k}) \right\rangle. \quad (\text{S37})$$

We apply the magnetic translation $\hat{t}_{\mathbf{L}_2}$ to these energy eigenstates. Note that they are eigenstates of $\hat{t}_{\mathbf{L}_1}$ and $\hat{t}_{\mathbf{L}_2}^q$; the reason why $\hat{t}_{\mathbf{L}_2}$ is applied q times is due to non-commuting nature of magnetic translation operators $\hat{t}_{\mathbf{L}_1}$ and $\hat{t}_{\mathbf{L}_2}$. We see that:

$$\begin{aligned} \hat{t}_{\mathbf{L}_2} \left| \Psi_a^{(\eta)}(\mathbf{k}) \right\rangle &= \sum_{n\gamma l} \sum_{r_2=0}^{p-1} U_{n\gamma l r_2, a}^{(\eta)}(\mathbf{k}) \hat{t}_{\mathbf{L}_2} \left| V_{n\gamma l}^{(\eta)}(k_1, k_2 + \frac{r_2}{q}) \right\rangle \\ &= \sum_{n\gamma l} \sum_{r_2=0}^{p-1} U_{n\gamma l r_2, a}^{(\eta)}(\mathbf{k}) e^{-i2\pi(k_2+r_2/q)} \left| V_{n\gamma l}^{(\eta)}(k_1 + p/q, k_2 + \frac{r_2}{q}) \right\rangle. \end{aligned} \quad (\text{S38})$$

Furthermore since $[H_{\text{non-int}}, \hat{t}_{\mathbf{L}_2}] = 0$, we have:

$$H_{\text{non-int}} \hat{t}_{\mathbf{L}_2} \left| \Psi_a^{(\eta)}(\mathbf{k}) \right\rangle = \hat{t}_{\mathbf{L}_2} H_{\text{non-int}} \left| \Psi_a^{(\eta)}(\mathbf{k}) \right\rangle = \varepsilon_a^{(\eta)}(\mathbf{k}) \hat{t}_{\mathbf{L}_2} \left| \Psi_a^{(\eta)}(\mathbf{k}) \right\rangle, \quad (\text{S39})$$

namely that $\hat{t}_{\mathbf{L}_2} \left| \Psi_a^{(\eta)}(\mathbf{k}) \right\rangle$ is an energy eigenstate at $([k_1 + p/q]_1, k_2)$.

This means that the tower of states are periodic with respect to $k_1 \rightarrow k_1 + 1/q$, and that all the distinct energy solutions can be found in the domain of $(k_1, k_2) \in [0, 1/q) \times [0, 1/q)$. Furthermore, the $\hat{t}_{\mathbf{L}_2}$ translation gives us one way of gauge fixing between k_1 values in different strips of $[0, 1/q)$. Specifically, we can define:

$$\left| \Psi_a^{(\eta)}([k_1 + p/q]_1, k_2) \right\rangle \equiv e^{i2\pi k_2} \hat{t}_{\mathbf{L}_2} \left| V_a(k_1, k_2) \right\rangle, \quad (\text{S40})$$

as the gauge-fixed eigenstate wavefunction at $([k_1 + p/q]_1, k_2)$. This amounts to the following definition:

$$U_{n\gamma l r, a}^{(\eta)}([k_1 + r_1 p/q]_1, k_2) = e^{-i2\pi r_1(r_2/q)} U_{n\gamma l r, a}^{(\eta)}(k_1, k_2), \quad r_1 = 0, \dots, q-1. \quad (\text{S41})$$

E. Matrix elements of $A_{\mathbf{q}} = \hat{A}e^{-i\mathbf{q}\cdot\mathbf{r}}$ with respect to narrow band eigenstates

This can be computed as follows:

$$\begin{aligned}
& \left\langle \Psi_a^{(\eta)}(\mathbf{k}) \left| A_{\mathbf{q}} \right| \Psi_b^{(\eta')}(\mathbf{p}) \right\rangle \\
&= \sum U_{n\gamma l r_2, a}^{(\eta)*}(\mathbf{k}) U_{n'\gamma' l' r'_2, b}^{(\eta')}(\mathbf{p}) \left\langle V_{n\gamma l}^{(\eta)}(k_1, k_2 + r_2/q) \left| A_{\mathbf{q}} \right| V_{n'\gamma' l'}^{(\eta')}(p_1, p_2 + r'_2/q) \right\rangle \\
&= \sum U_{n\gamma l r_2, a}^{(\eta)*}(\mathbf{k}) U_{n'\gamma' l' r'_2, b}^{(\eta')}(\mathbf{p}) \delta_{[p_1 - k_1 - q_1]_1, 0} \\
&\quad \times \sum_s \delta_{p_2 - sp/q, k_2 + q_2} e^{i2\pi(p_1 - p_2 \frac{L_1 y}{L_2})s} e^{i\frac{s^2}{2}\mathbf{q}\cdot\mathbf{L}_1} e^{-isK_{n'\gamma' l', x} L_{1, x}} e^{i\tilde{q}_x \tilde{k}_2, n l \ell^2} e^{i\frac{1}{2}\tilde{q}_x \tilde{q}_y \ell^2} \hat{A}_{n\gamma l, n'\gamma' l'}^{\eta\eta'}.
\end{aligned} \tag{S42}$$

Note that here the δ -constraint depends on r_2, r'_2 , and matrix elements are only non-vanishing for:

$$\mathbf{q} = \mathbf{p} - \mathbf{k} + \frac{r'_2 - r_2}{q} \mathbf{g}_2 + r \mathbf{g}_1 - \frac{sp}{q} \mathbf{g}_2. \tag{S43}$$

Computing above brute-force is costly. However we could make use of $\hat{t}_{\mathbf{L}_2}$ to reduce the amount of calculations by a factor of $q^2/(2q-1)$. This is seen by noting that:

$$\begin{aligned}
& \left\langle V_{n\gamma l}^{(\eta)}([k_1 + r_1 p/q]_1, k_2) \left| A_{\mathbf{q}} \right| V_{n\gamma l}^{(\eta)}([p_1 + r_1 p/q]_1, p_2) \right\rangle \\
&= e^{i2\pi r_1(p_2 - k_2)} \left\langle V_{n\gamma l}^{(\eta)}(\mathbf{k}) \left| \hat{t}_{\mathbf{L}_2}^{-r_1} A_{\mathbf{q}} \hat{t}_{\mathbf{L}_2}^{r_1} \right| V_{n'\gamma' l'}^{(\eta)}(\mathbf{p}) \right\rangle \\
&= e^{i2\pi r_1(p_2 - k_2 - q_2)} \left\langle V_{n\gamma l}^{(\eta)}(\mathbf{k}) \left| A_{\mathbf{q}} \right| V_{n'\gamma' l'}^{(\eta)}(\mathbf{p}) \right\rangle \\
&= e^{-i2\pi r_1 n/q} \left\langle V_{n\gamma l}^{(\eta)}(\mathbf{k}) \left| A_{\mathbf{q}} \right| V_{n'\gamma' l'}^{(\eta)}(\mathbf{p}) \right\rangle, \quad n \in \mathbb{Z}.
\end{aligned} \tag{S44}$$

In the last step we made use of the constraint $q_2 = p_2 - k_2 + n/q$. Therefore, rather than calculating q^2 blocks of matrices corresponding to differences in k_1, p_1 , we only need to compute $2q-1$ blocks, and generate all remaining ones by multiplying a global phase factor.

III. SELF-CONSISTENT HARTREE-FOCK METHOD IN FINITE MAGNETIC FIELD

We proceed to discuss the Hartree-Fock procedure in a finite magnetic field (B-SCHF). We consider the strained BM Hamiltonian in the presence of screened Coulomb interactions, and project it onto the finite field Hilbert space. The Hamiltonian is given by:

$$H = \sum_{\eta s a, \mathbf{k}} \varepsilon_{sa}^{(\eta)}(\mathbf{k}) d_{\eta s a, \mathbf{k}}^\dagger d_{\eta s a, \mathbf{k}} + \frac{1}{2A} \sum_{\mathbf{q}} V_{\mathbf{q}} \delta \hat{\rho}_{\mathbf{q}} \delta \hat{\rho}_{-\mathbf{q}}, \tag{S45}$$

where A is the area of the system, $\varepsilon_{sa}^{(\eta)}(\mathbf{k})$ is the Hofstadter spectra including spin Zeeman splitting, and $V_{\mathbf{q}}$ is the Fourier transform of the screened Coulomb interaction. The projected density operator is given by:

$$\delta \hat{\rho}_{\mathbf{q}} = \sum_{\eta s} \left\langle \Psi_a^{(\eta)}(\mathbf{k}) \left| \hat{\rho} e^{-i\mathbf{q}\cdot\mathbf{r}} \right| \Psi_b^{(\eta)}(\mathbf{p}) \right\rangle \left(d_{\eta s a, \mathbf{k}}^\dagger d_{\eta s b, \mathbf{p}} - \frac{1}{2} \delta_{a, b} \delta_{\mathbf{k}, \mathbf{p}} \right) \tag{S46}$$

where $\hat{\rho} = \hat{I}$. We emphasize again that the matrix elements are non-zero only for wavevectors satisfying:

$$\mathbf{q} = \mathbf{p} - \mathbf{k} + \frac{r'_2 - r_2}{q} \mathbf{g}_2 + r \mathbf{g}_1 - \frac{sp}{q} \mathbf{g}_2. \tag{S47}$$

Here on we introduce the matrix notation for the structure factor:

$$\hat{\Lambda}_{\mathbf{q}}^{\eta s}(a\mathbf{k}, b\mathbf{p}) \equiv \left\langle \Psi_a^{(\eta)}(\mathbf{k}) \left| \hat{\rho} e^{-i\mathbf{q}\cdot\mathbf{r}} \right| \Psi_b^{(\eta)}(\mathbf{p}) \right\rangle. \tag{S48}$$

where we use s to label spin. Pay attention that in prior contexts we have used s to denote an integer.

As a result, the Coulomb piece of the Hamiltonian can be written as:

$$H_U = \frac{1}{2A} \sum_{\mathbf{q}} V_{\mathbf{q}} \hat{\Lambda}_{\mathbf{q}}^{\eta s}(a\mathbf{k}, b\mathbf{p}) \hat{\Lambda}_{\mathbf{q}}^{\eta' s' *}(\beta\mathbf{p}', \alpha\mathbf{k}') \left(d_{\eta s a, \mathbf{k}}^{\dagger} d_{\eta s b, \mathbf{p}} - \frac{1}{2} \delta_{a,b} \delta_{\mathbf{k}, \mathbf{p}} \delta_{\mathbf{q}, \mathbf{G}} \right) \left(d_{\eta' s' \alpha, \mathbf{k}'}^{\dagger} d_{\eta' s' \beta, \mathbf{p}'} - \frac{1}{2} \delta_{\alpha, \beta} \delta_{\mathbf{k}', \mathbf{p}'} \delta_{\mathbf{q}, \mathbf{G}} \right), \quad (\text{S49})$$

where $\mathbf{G} = m\mathbf{g}_1 + n\mathbf{g}_2$ is the moiré reciprocal lattice vector. We note first on the constraint of the δ -functions on the allowed values of momentum. Specifically we have:

$$\mathbf{q} = \mathbf{p} - \mathbf{k} + m\mathbf{g}_1 + \frac{n}{q}\mathbf{g}_2 = \mathbf{k}' - \mathbf{p}' + m'\mathbf{g}_1 + \frac{n'}{q}\mathbf{g}_2. \quad (\text{S50})$$

Since $p_1 - k_1 \in (-1, 1)$ and $p_2 - k_2 \in (-1/q, 1/q)$, the following constraint applies:

$$\mathbf{p} - \mathbf{k} = \mathbf{k}' - \mathbf{p}', \quad m = m', \quad n = n'. \quad (\text{S51})$$

A. Product state and one-particle density matrix

At a given filling, we consider a ground state $|\Omega\rangle$ to be a product state, given by partial fillings of the narrow band states $|\Psi_a^{\eta s}(\mathbf{k})\rangle$. This is equivalent to defining a one-particle density matrix:

$$\hat{Q}_{a,b}^{\eta s, \eta' s'}(\mathbf{k}) \equiv \langle \Omega | d_{\eta s a, \mathbf{k}}^{\dagger} d_{\eta' s' b, \mathbf{k}} | \Omega \rangle - \frac{1}{2} \delta_{\eta, \eta'} \delta_{s, s'} \delta_{a,b}. \quad (\text{S52})$$

Note that $\hat{t}_{\mathbf{L}_2}$ takes \mathbf{k} to $\mathbf{k} + \phi/\phi_0\mathbf{g}_1$, and as a result, a difference of the density matrix at $\hat{Q}(\mathbf{k})$ and $\hat{Q}(\mathbf{k} + \phi/\phi_0\mathbf{g}_1)$ allows us to probe magnetic translation symmetry breaking of $\hat{t}_{\mathbf{L}_2}$.

B. Hartree Fock Hamiltonian

The Hartree-Fock Hamiltonian is given as:

$$H^{HF} = \frac{1}{A} \sum_{\mathbf{q}} V_{\mathbf{q}} \hat{\Lambda}_{\mathbf{q}}^{\eta s}(a\mathbf{k}, b\mathbf{k}) \hat{\Lambda}_{\mathbf{q}}^{\eta' s' *}(\beta\mathbf{k}', \alpha\mathbf{k}') \hat{Q}_{\alpha, \beta}^{\eta' s', \eta' s'}(\mathbf{k}') \left(d_{\eta s a, \mathbf{k}}^{\dagger} d_{\eta s b, \mathbf{k}} - \frac{1}{2} \delta_{a,b} \right) - \frac{1}{A} \sum_{\mathbf{q}} V_{\mathbf{q}} \hat{\Lambda}_{\mathbf{q}}^{\eta s}(a\mathbf{k}, b\mathbf{p}) (\hat{Q}^T)_{b, \alpha}^{\eta s, \eta' s'}(\mathbf{p}) \hat{\Lambda}_{\mathbf{q}}^{\eta' s' \dagger}(\alpha\mathbf{p}, \beta\mathbf{k}) \left(d_{\eta s a, \mathbf{k}}^{\dagger} d_{\eta' s' \beta, \mathbf{k}} - \frac{1}{2} \delta_{a, \beta} \delta_{\eta, \eta'} \delta_{s, s'} \right). \quad (\text{S53})$$

Our B-SCHF results are obtained by minimizing Eq. S53 with respect to product state $|\Omega\rangle$. In practice, we achieve minimization by running both random initializations for the density matrix \hat{Q} as well as for educated guesses, such as a strong coupling Chern insulating state, flavor polarized state, intervalley coherent state, etc. Typically, the phase diagram obtained in Fig. 1 of the main text is a collection of up to 10 initializations schemes of the density matrix.

For each magnetic flux ratio ϕ/ϕ_0 , we study momentum space mesh consisting of $n_q q$ points along \mathbf{g}_1 direction in the range of $[0, 1)$, and n_q points along \mathbf{g}_2 direction in the range of $[0, 1/q)$, where n_q is chosen as the maximum integer such that $n_q q \leq 14$. Our calculations presented in the main text correspond to 23 magnetic flux ratios between $1/12$ and $1/2$, where we take $q \leq 12$ and $p < q$.

IV. EXTENDED FIGURES

A. Extended results in the presence of heterostrain

Here we present B-SCHF results obtained for various twist angles in the presence of heterostrain.

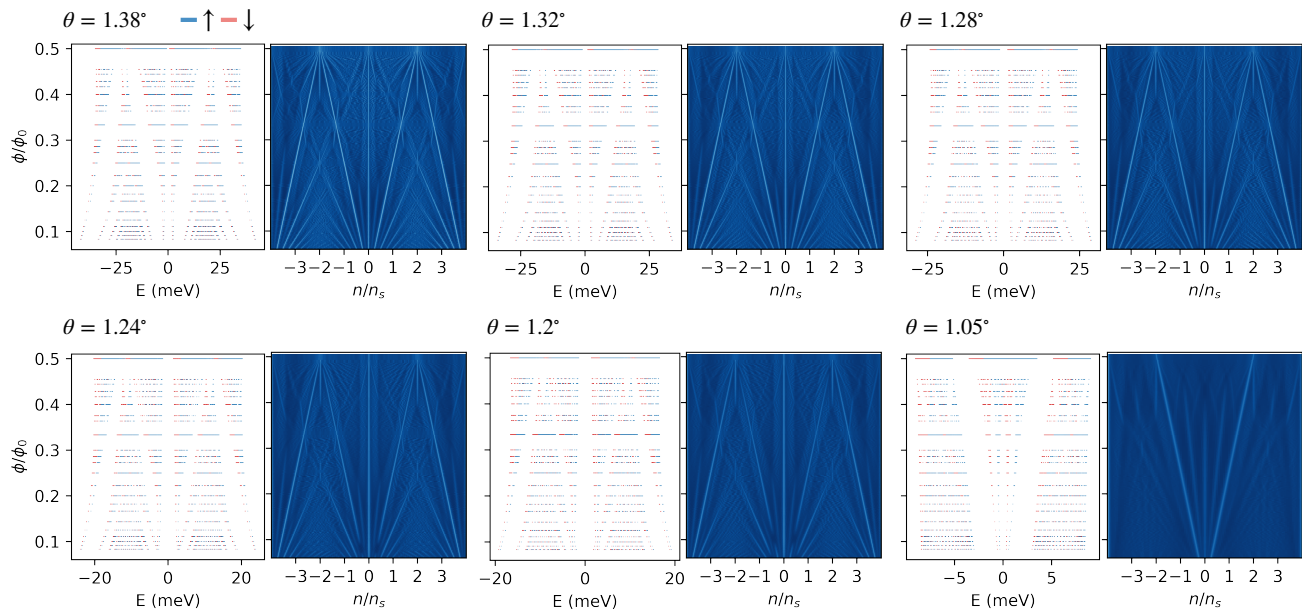


FIG. S1. Non-interacting Hofstadter spectra and Wannier plots for various twist angles with heterostrain. In the Wannier plots, bright colors correspond to low density of states (gapped) and darker blue colors corresponds to high density of states (compressible). In obtaining the Wannier plots we used an energy broadening factor of $\gamma = 0.1\text{meV}$.

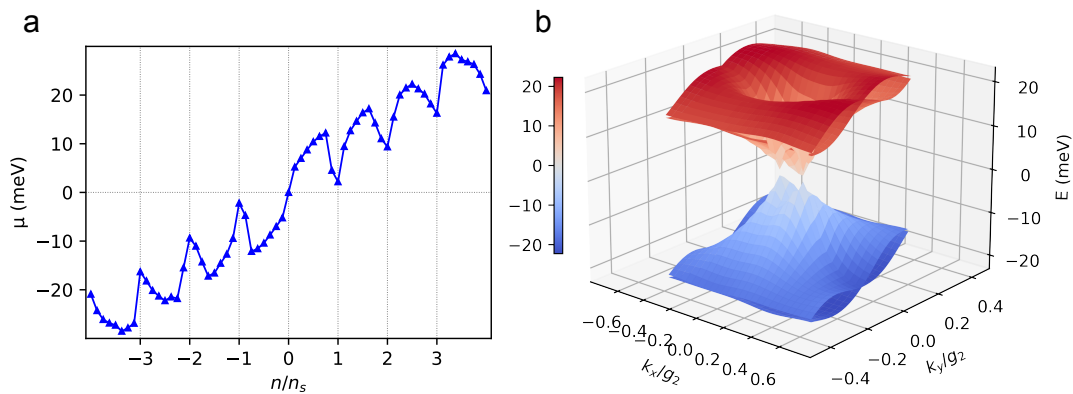


FIG. S2. (a) Chemical potential μ versus filling n/n_s for $\theta = 1.05^\circ$, zero magnetic field, and with heterostrain. Results obtained for 16×16 mesh. (b) 3D plot of Hartree-Fock renormalized energy dispersions at $n/n_s = 0$ for the same parameterization, showing semimetallic behavior. Dispersion obtained for 25×25 mesh.

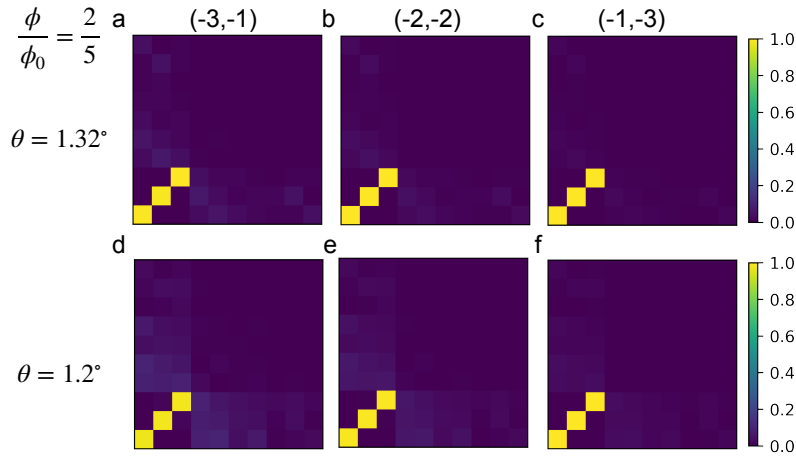


FIG. S3. Absolute values of the density matrices at $\mathbf{k} = \mathbf{0}$ of an occupied valley/spin flavor for the correlated Hofstadter ferromagnets (CHF), expressed in the eigenbasis of $(0, -4)$. Results are obtained at flux ratio $\phi/\phi_0 = 2/5$ and in the presence of heterostrain. Here we show that the CHF are flavor symmetry breaking states that predominantly occupy the lower Chern -1 group of renormalized magnetic subbands obtained at $(0, -4)$.

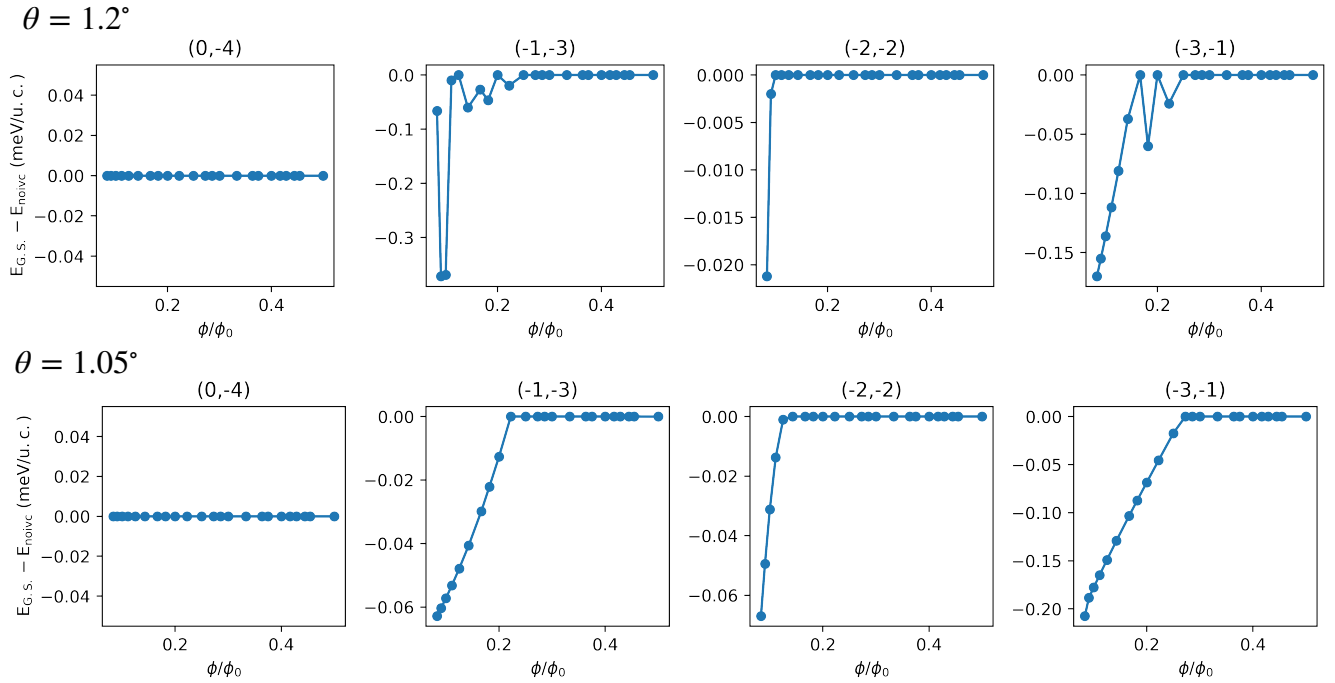


FIG. S4. Differences of Hartree-Fock energies per moiré unit cell between the true ground state $E_{G.S.}$ and the minimum energy state without intervalley coherence E_{noivc} at twist angles 1.2° (upper panel) and 1.05° (lower panel) with heterostrain for $(s, t) = (0, -4)$, $(-1, -3)$, $(-2, -2)$, and $(-3, -1)$. This figure complements Fig. 2 of the main text, which shows that at lower magnetic flux ratios, there is a first order phase transition from a CHF to a gapped state with intervalley coherence. The non-monotonicity of the energy differences as a function of magnetic flux is attributed to finite size effects, where different momentum space discretizations are employed for magnetic flux ratios $\phi/\phi_0 = p/q$ with different values of q .

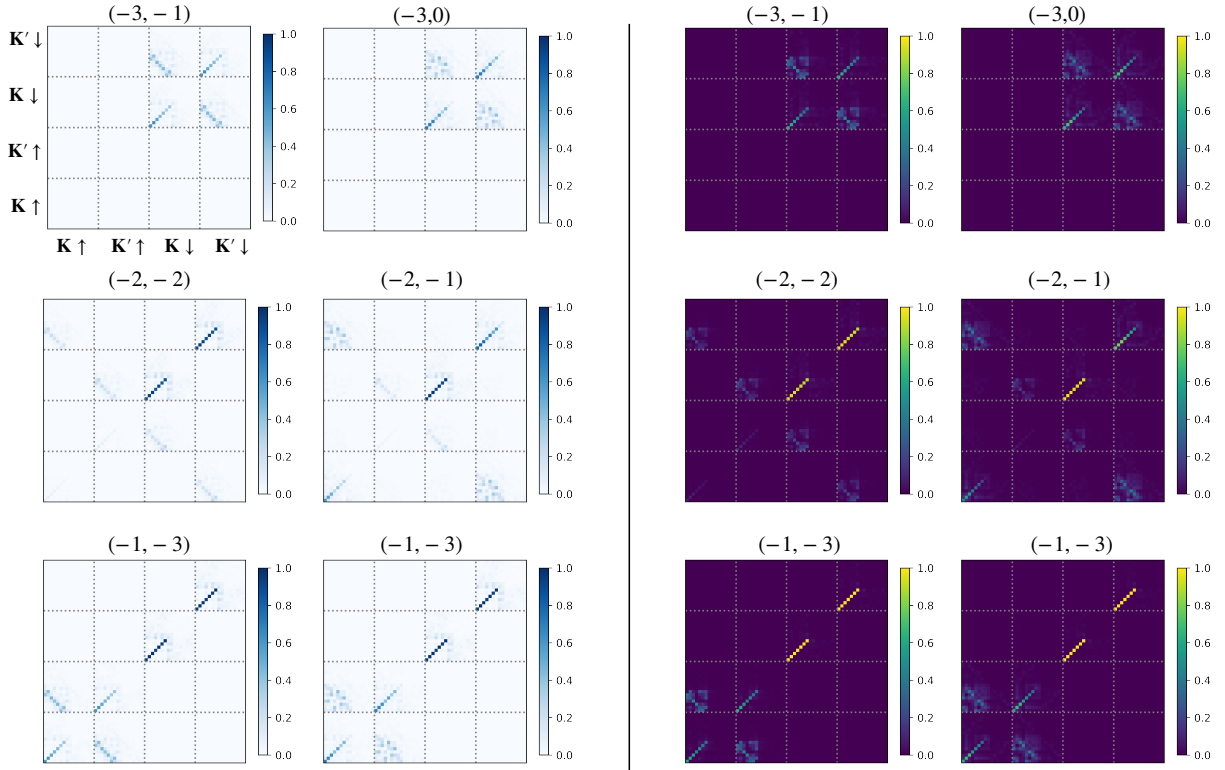


FIG. S5. Absolute values of the full density matrices at $\mathbf{k} = \mathbf{0}$ for the intervalley coherent states at $(-3, -1)$, $(-2, -2)$ and $(-1, -3)$, as well as $(-3, 0)$, $(-2, -1)$ and $(-1, -2)$. Results obtained for $\theta = 1.05^\circ$, $\phi/\phi_0 = 1/8$, and with heterostrain. Left panels are density matrices expressed in the non-interacting Hofstadter basis, whereas right panels are the same density matrices but expressed in the eigenbasis of $(0, -4)$.

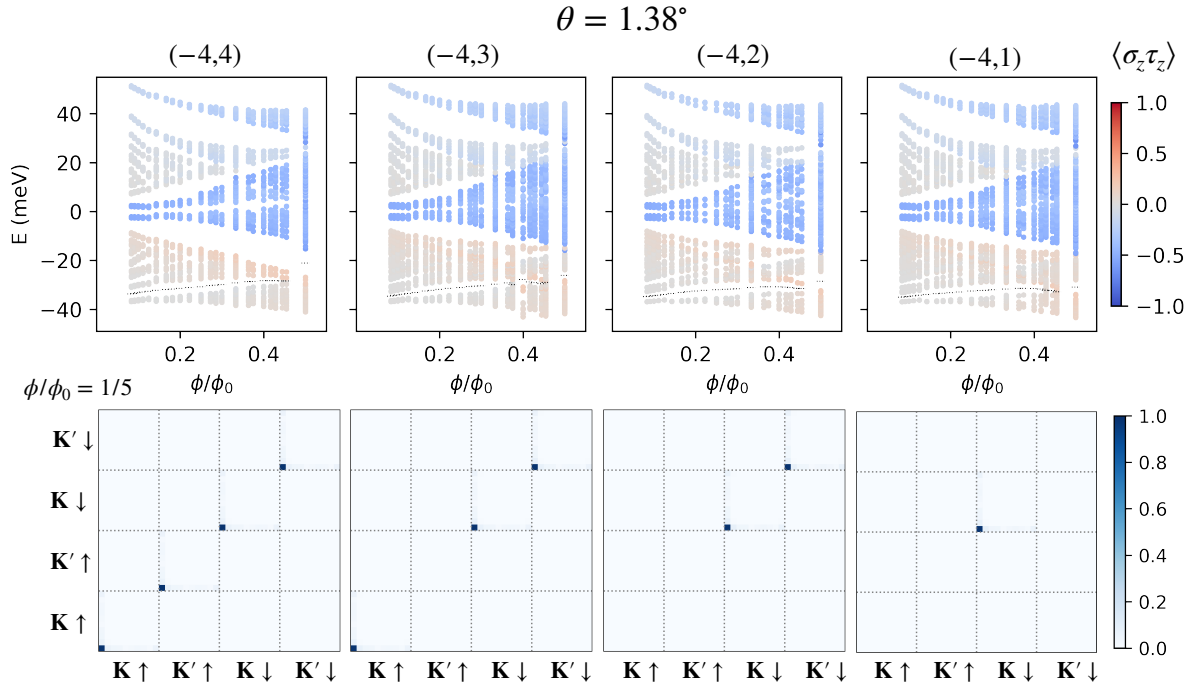


FIG. S6. B-SCHF spectra (upper panel) and the absolute values of the respective density matrices at $\mathbf{k} = \mathbf{0}$ (lower panel) for QHFM emanating from band bottom, described by Streda lines $(s, t) = (-4, 4)$, $(-4, 3)$, $(-4, 2)$, and $(-4, 1)$ (lower panels). Electronic states below the dashed lines are occupied. Results are obtained at twist angle $\theta = 1.38^\circ$, and with heterostrain. The density matrices are obtained at $\phi/\phi_0 = 1/5$. They are predominantly valley/spin polarizations of the zeroth LL emanating from non-interacting band bottom, without intervalley coherence. The qualitative behaviors are the same for all twist angles studied.

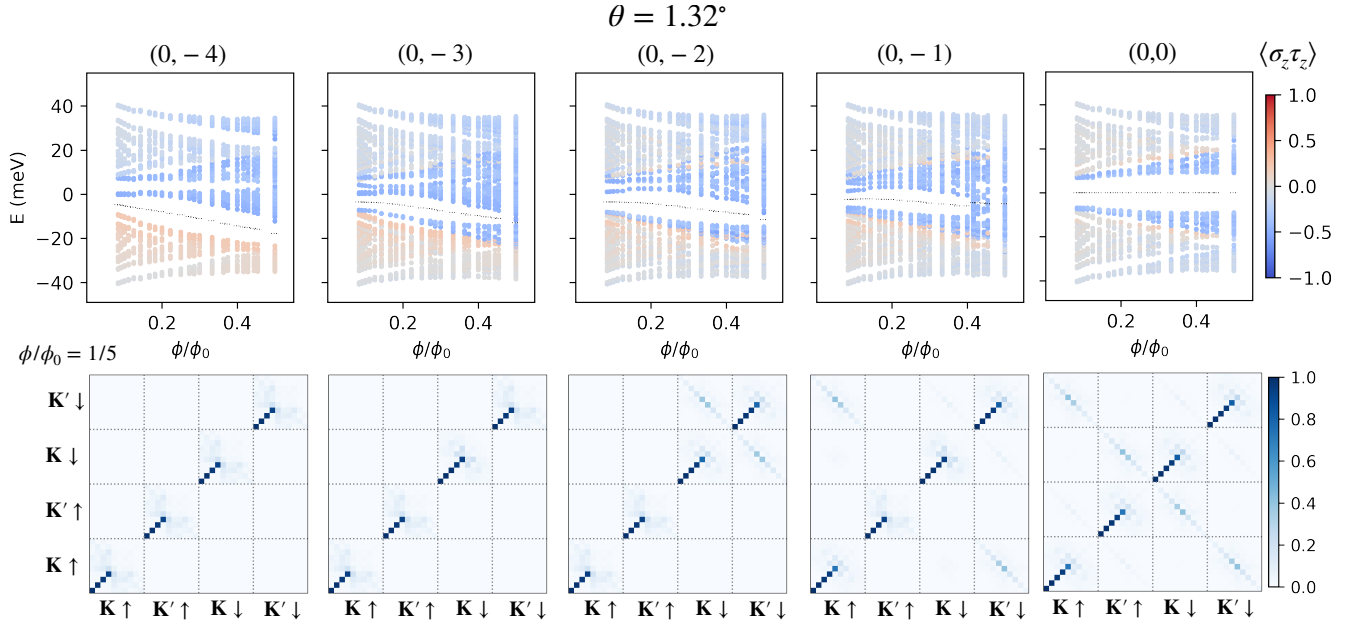


FIG. S7. B-SCHF spectra (upper panel) and the absolute values of the respective density matrices at $\mathbf{k} = \mathbf{0}$ (lower panel) for QHFM emanating from the charge neutrality point, described by Streda lines $(s, t) = (0, -4)$, $(0, -3)$, $(0, -2)$, $(0, -1)$, and $(0, 0)$ (lower panels). Electronic states below the dashed lines are occupied. Results obtained at twist angle $\theta = 1.32^\circ$, and with heterostrain. The density matrices are obtained at $\phi/\phi_0 = 1/5$. Note that QHFM from charge neutrality point are predominantly associated with the zeroth LLs of the Dirac points, and develop intervalley coherence, in contrast to QHFM from band bottom. The qualitative behaviors are the same for all twist angles studied.

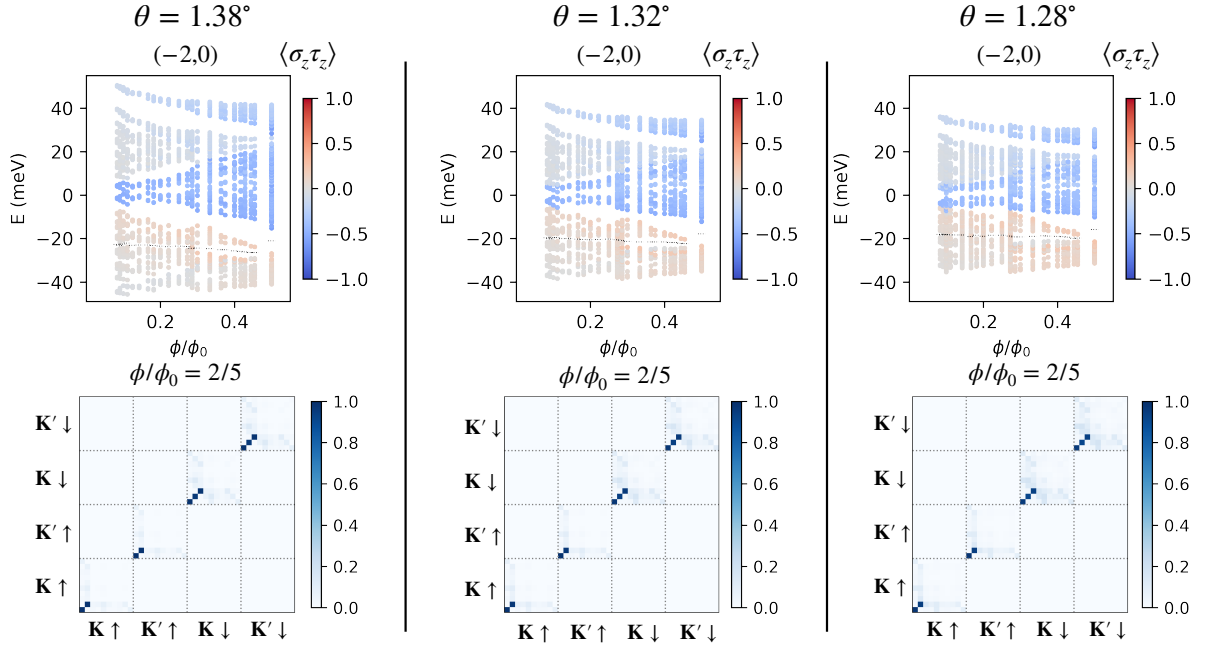


FIG. S8. Gapped states along $(-2, 0)$ at higher magnetic flux ratios for 1.38° , 1.32° and 1.28° (upper panel), as well as the absolute values of the representative density matrices at $\mathbf{k} = \mathbf{0}$ at $\phi/\phi_0 = p/q = 2/5$ (lower panel). Electronic states below the dashed lines are occupied. These states are adiabatically connected to the non-interacting Quantum Spin Hall insulators shown in the Wannier diagrams of Fig. S1, where the magnetic subband group developed from the lowest LL for the up spin sector (p diagonal squares at the lower left corner of the density matrix for a given valley/spin flavor), and the magnetic subband group below the zeroth LL near charge neutrality for the down spin sector ($q - p$ diagonal squares at the lower left corner of the density matrix for a given valley/spin flavor), are occupied.

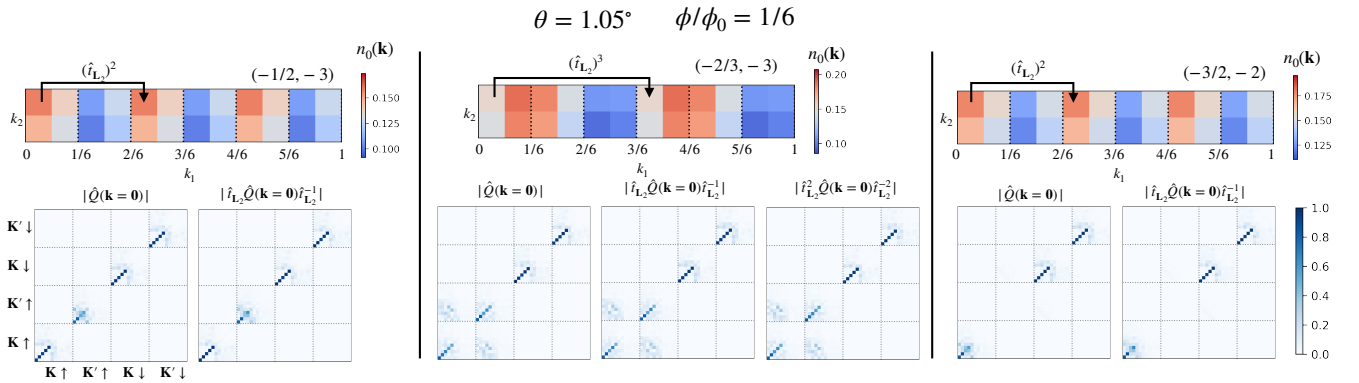


FIG. S9. Examples of CCIs with fractional s . Results obtained at 1.05° and $\phi/\phi_0 = 1/6$ with heterostrain. $n_0(\mathbf{k})$ is the occupation number of the zeroth LL emanating from the Dirac points of the non-interacting spectra, in the same notation as Fig. 4 of the main text.

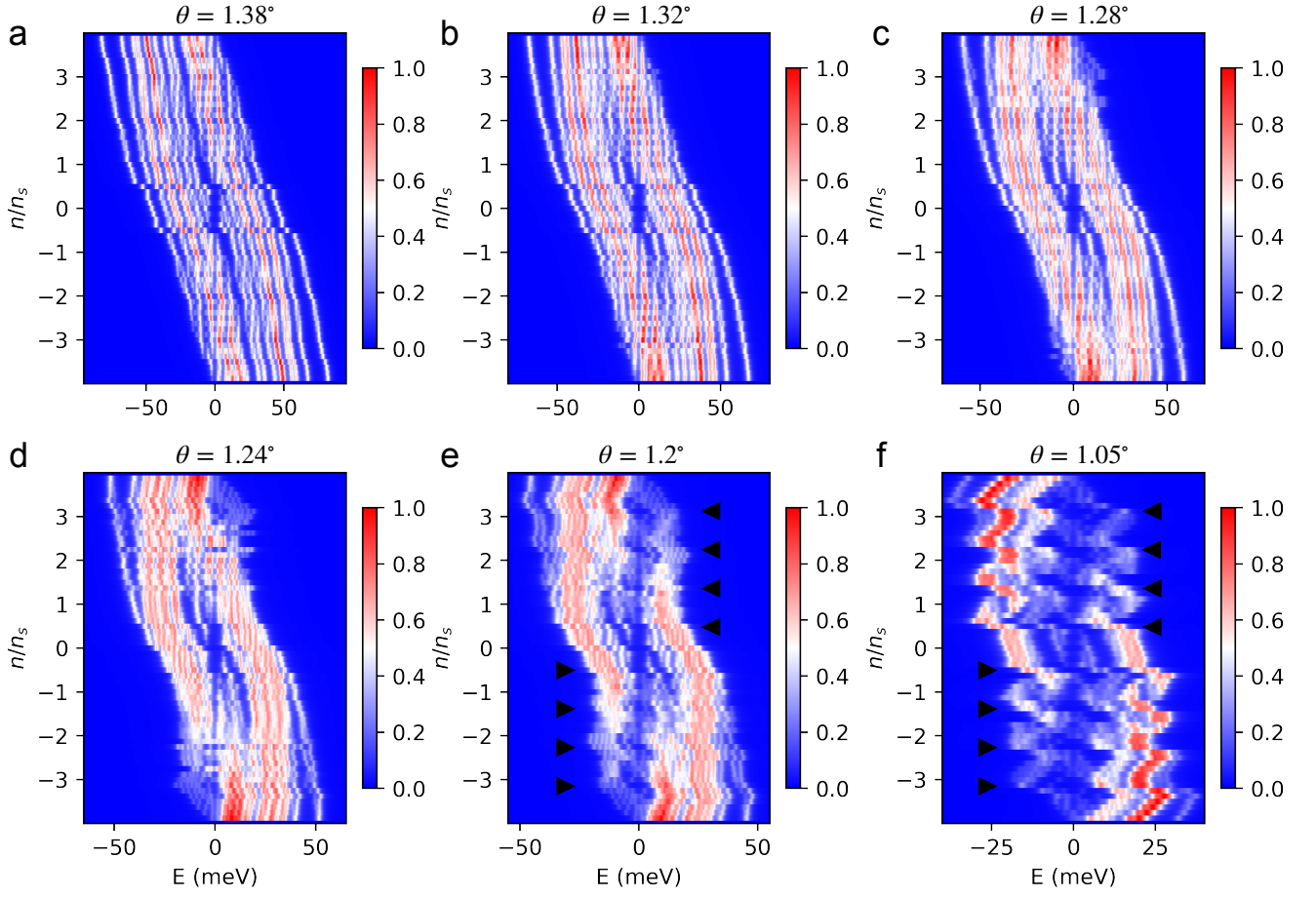


FIG. S10. Calculated density of states $\mathcal{N}(E) \propto \frac{1}{\pi} \sum_i \frac{\gamma}{\gamma^2 + (E - \epsilon_i)^2}$ at $\phi/\phi_0 = 1/8$ for various twist angles and with heterostrain. $\mathcal{N}(E)$ is normalized with respect to the maximum value. $E = 0$ corresponds to the position of the chemical potential μ at a given filling n/n_s . Here we used an energy broadening factor of $\gamma = 1\text{meV}$. Dark arrows in (e) and (f) mark electron densities at $(s, t) = (0, \pm 4), \pm(1, 3), \pm(2, 2), \pm(3, 1)$.

B. Extended results in the absence of heterostrain

Here we present B-SCHF results obtained for various twist angles in the absence of heterostrain.

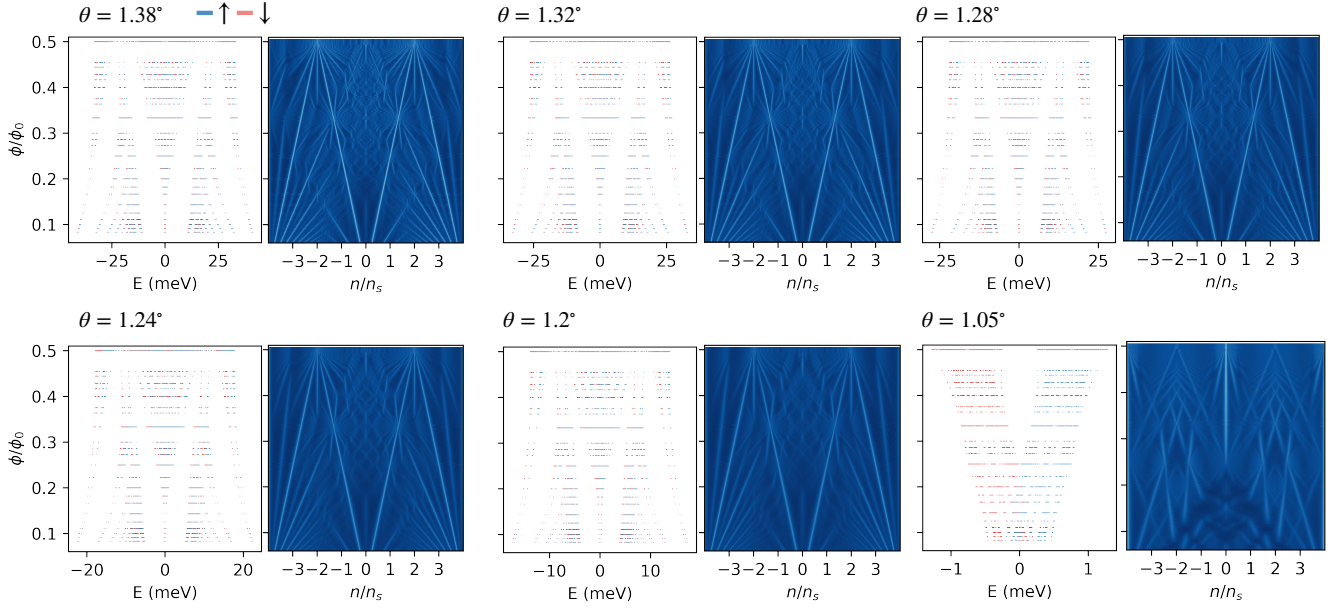


FIG. S11. Non-interacting Hofstadter spectra and Wannier plots for various twist angles without heterostrain. In the Wannier plots, bright colors correspond to low density of states (gapped) and darker blue colors correspond to high density of states (compressible). In obtaining the Wannier plots we used an energy broadening factor of $\gamma = 0.1\text{meV}$, with the exception of 1.05° where we used $\gamma = 0.01\text{meV}$.

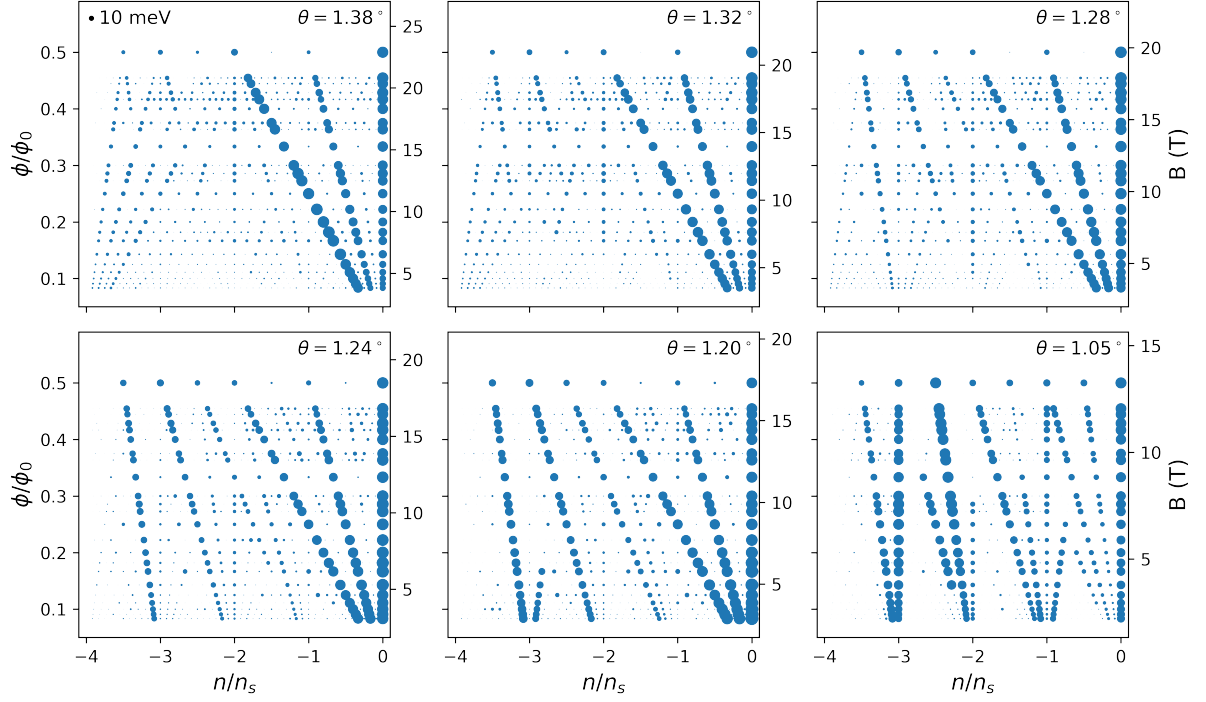


FIG. S12. B-SCHF results for the single-electron excitation gap as a function of filling (n/n_s) and magnetic flux ratio (ϕ/ϕ_0) for various twist angles in the absence of heterostrain. Due to near energetic degeneracies of various competing phases close to the magic angle, the phase diagram at 1.05° presented here can be sensitive to kinetic energy terms beyond the Bistritzer-MacDonald Hamiltonian.

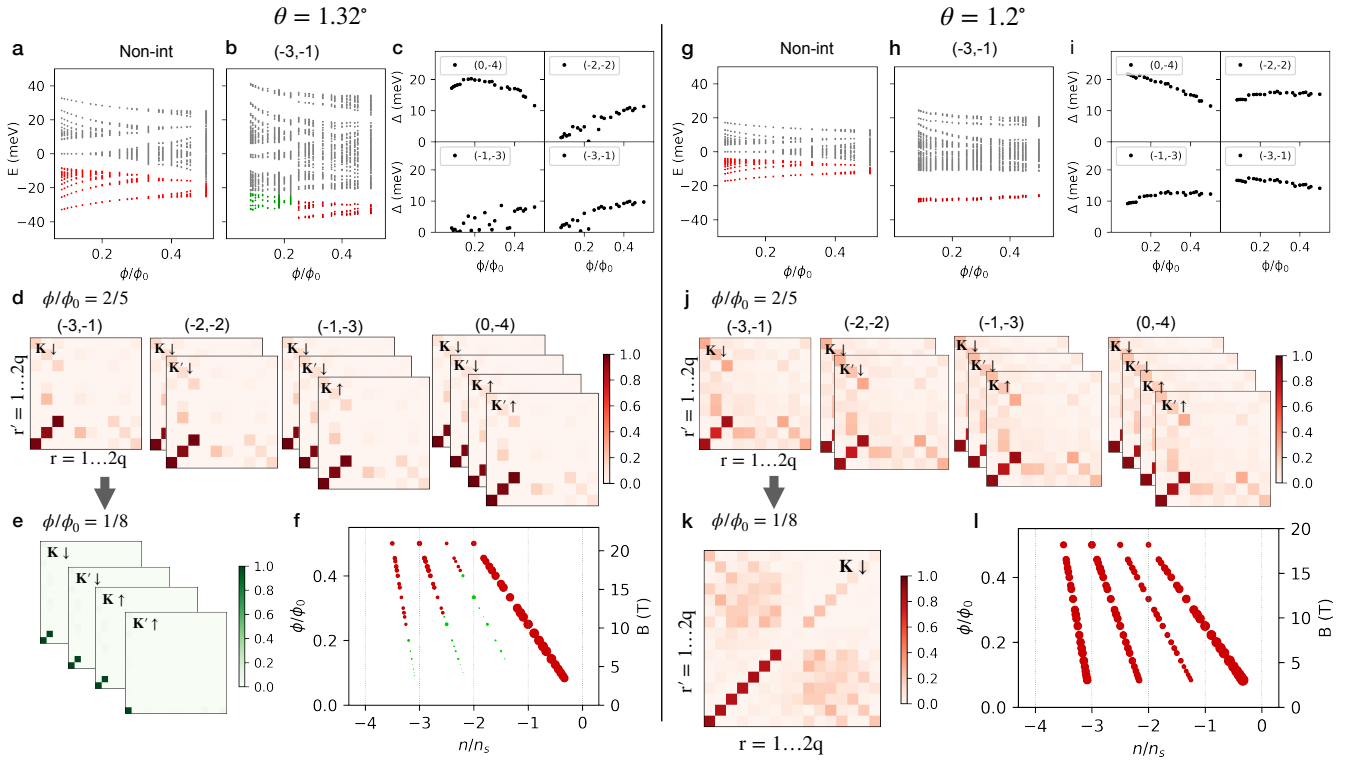


FIG. S13. Detailed results for the main sequence of CCIs at 1.32° and 1.2° twist angles in the absence of heterostrain. The results are to be contrasted with Fig. 2 of the main text. Notably at 1.2° , the CHFs are stable down to the lowest magnetic flux ratio $\phi/\phi_0 = 1/12$ studied, without nearby competing states.

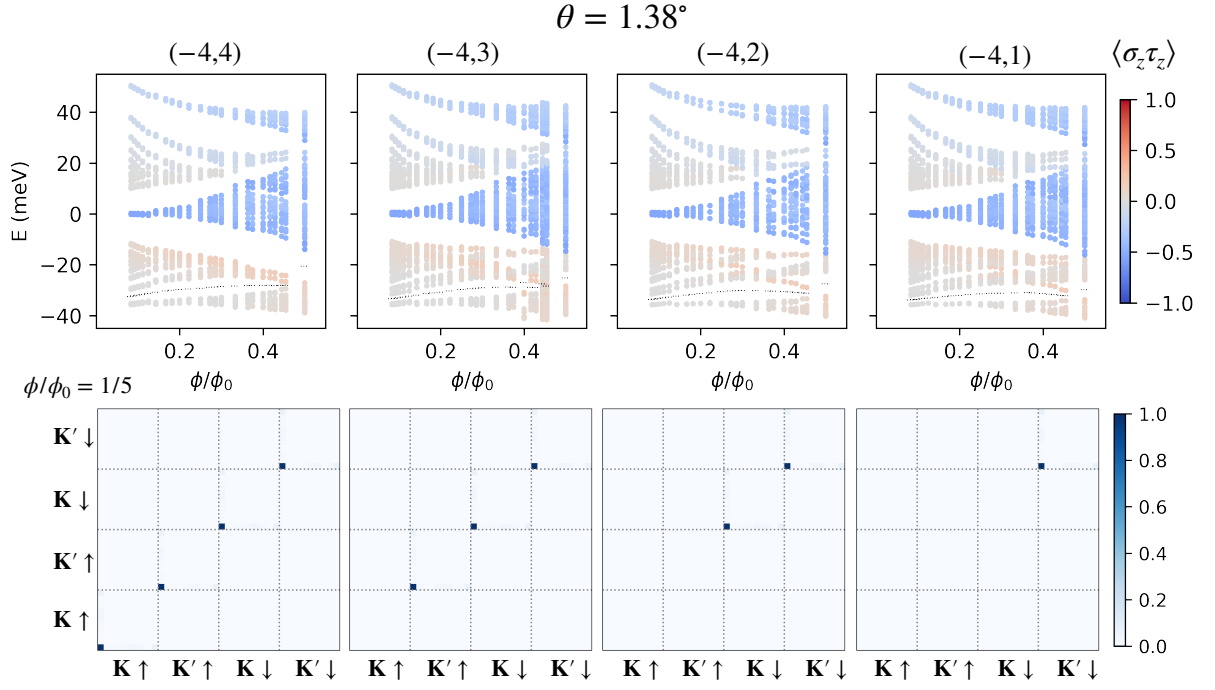


FIG. S14. B-SCHF spectra (upper panel) and the absolute values of the respective density matrices at $\mathbf{k} = \mathbf{0}$ (lower panel) for QHFM emanating from band bottom, described by Streda lines $(s, t) = (-4, 4)$, $(-4, 3)$, $(-4, 2)$, and $(-4, 1)$ (lower panels). Electronic states below the dashed lines are occupied. Results obtained at the higher twist angle $\theta = 1.38^\circ$, and without heterostrain. The density matrices are obtained at $\phi/\phi_0 = 1/5$. They are predominantly valley/spin polarizations of the zeroth LL emanating from non-interacting band bottom, without intervalley coherence. The qualitative behaviors are the same for all twist angles.

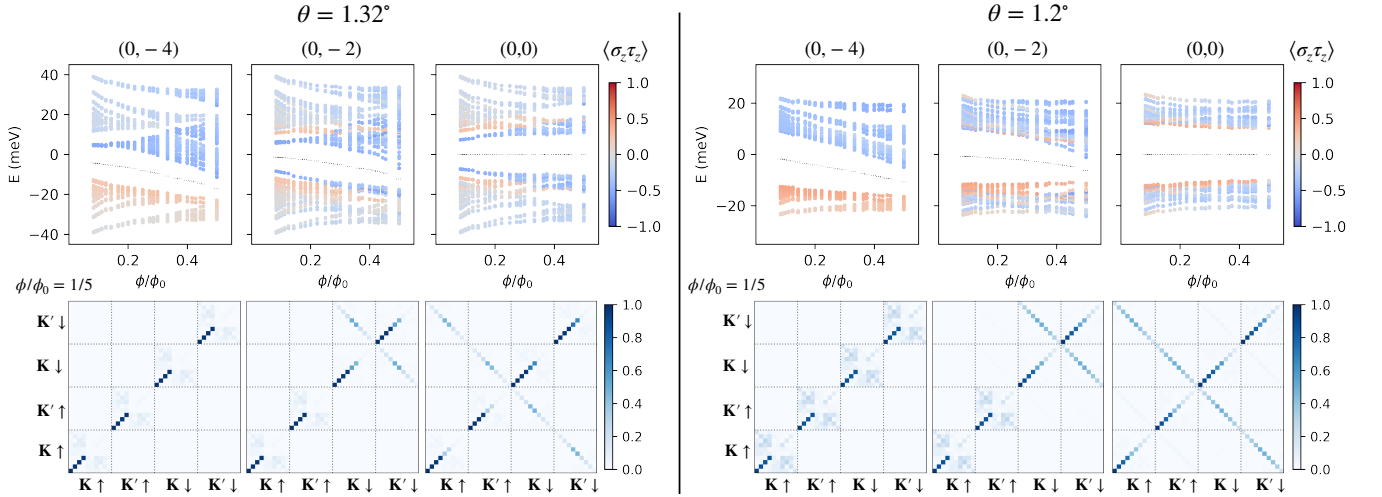


FIG. S15. B-SCHF spectra (upper panel) and the absolute values of the respective density matrices at $\mathbf{k} = \mathbf{0}$ (lower panel) for QHFM emanating from the charge neutrality point, described by Streda lines $(s, t) = (0, -4)$, $(0, -2)$, and $(0, 0)$ (lower panels). Electronic states below the dashed lines are occupied. Results obtained at twist angles $\theta = 1.32^\circ$ and 1.2° , and without heterostrain. The density matrices are obtained at $\phi/\phi_0 = 1/5$. Note that QHFM from charge neutrality point are predominantly associated with the zeroth LLs of the Dirac points, and develop intervalley coherence, in contrast to QHFM from band bottom. The qualitative behaviors are the same for all twist angles.

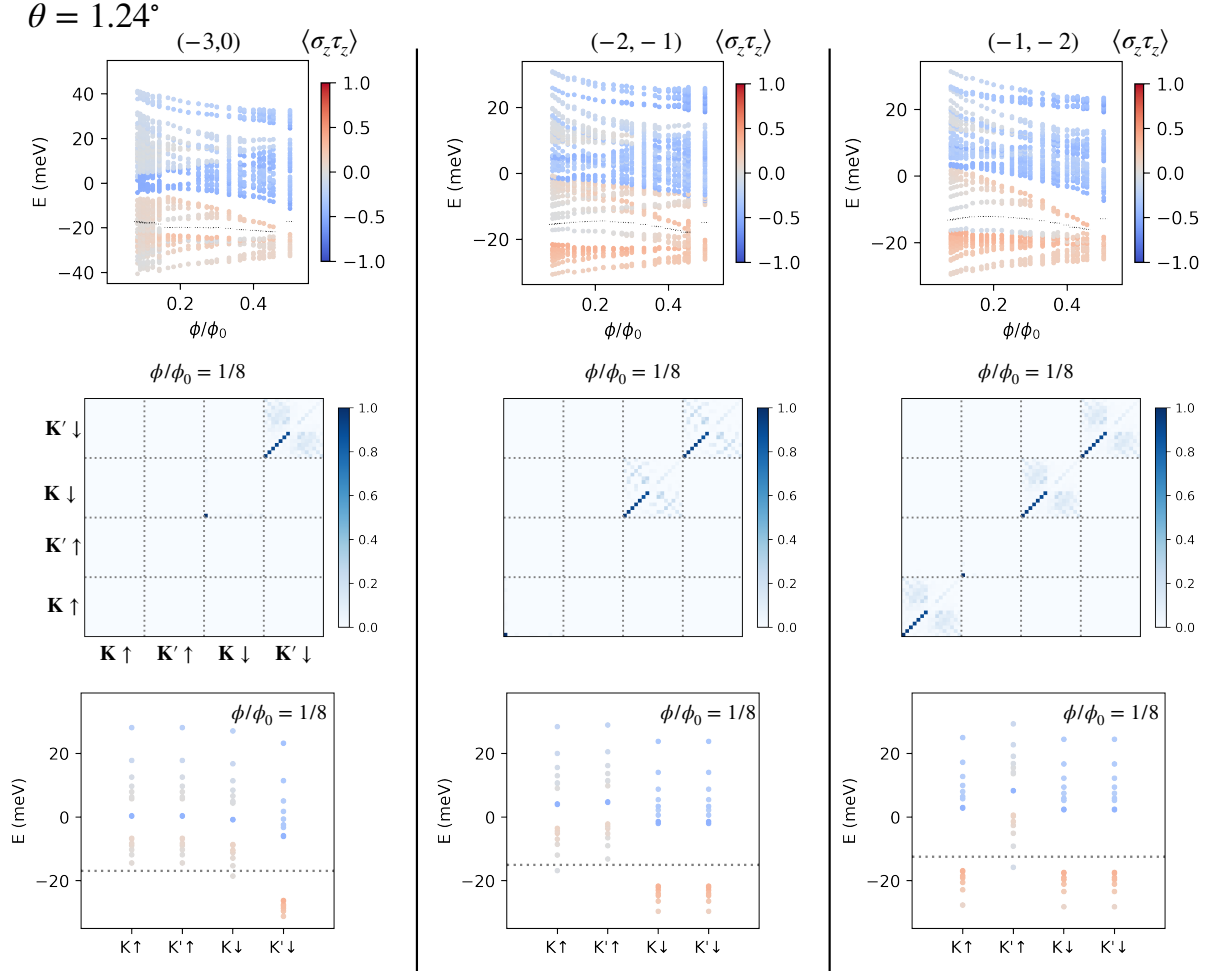


FIG. S16. B-SCHF spectra (upper panel), representative density matrix $|\hat{Q}_{\eta sr, \eta' s' r'}(\mathbf{k} = \mathbf{0})|$ at $\phi/\phi_0 = 1/8$ (middle panel) and flavor resolved spectra (lower panel), described by Streda lines $(s, t) = (-3, 0)$, $(-2, -1)$, and $(-1, -2)$. Electronic states below the dashed lines are occupied. These are secondary CCIs with a +1 higher Chern number than the main CCIs along $(-3, -1)$ $(-2, -2)$ $(-1, -3)$. Results obtained at $\theta = 1.24^\circ$, and without heterostrain. Unlike results with heterostrain (see Fig. S5), here these states do not exhibit intervalley coherence. Rather, the middle and lower panels clearly demonstrate that the one extra Chern number compared to the main CCIs at $(-3, -1)$, $(-2, -2)$, and $(-1, -3)$ comes from populating the one zeroth LL from the band bottom.

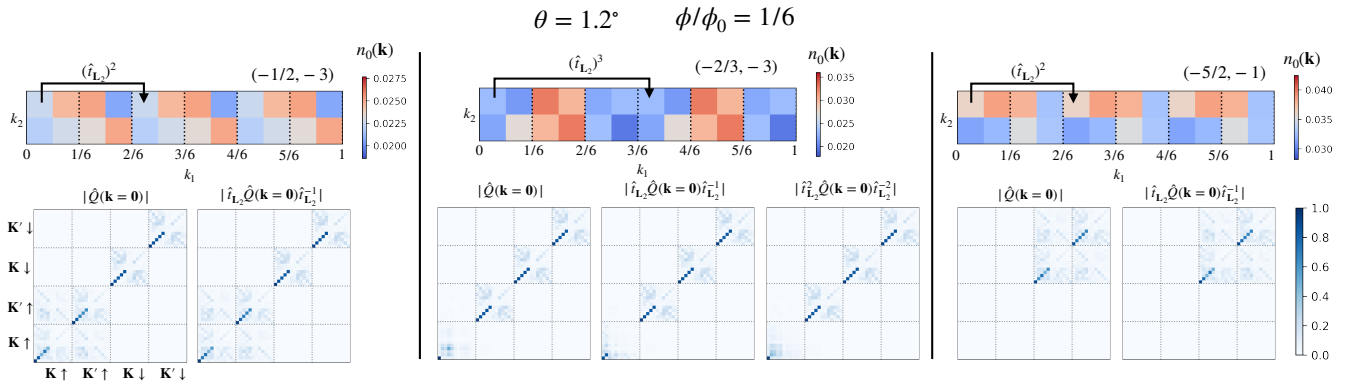


FIG. S17. Examples of CCIs with fractional s . Results are obtained at 1.2° , $\phi/\phi_0 = 1/5$, and without heterostrain. $n_0(\mathbf{k})$ is the occupation number of the zeroth LL emanating from the Dirac points of the non-interacting spectra, in the same notation as Fig. 4 of the main text.

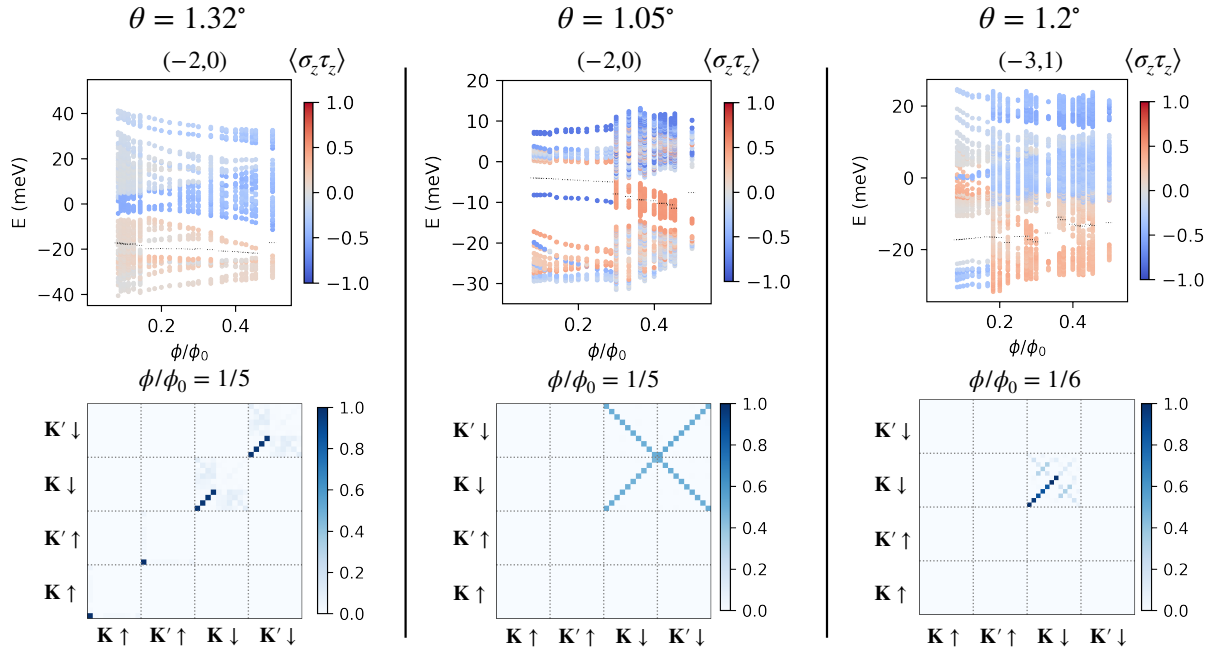


FIG. S18. Additional correlated insulating states in magnetic phase diagram in Fig. S12 along $(-2, 0)$ for 1.32° and 1.05° , as well as the $(-3, 1)$ gapped state for 1.2° . Electronic states below the dashed lines are occupied.

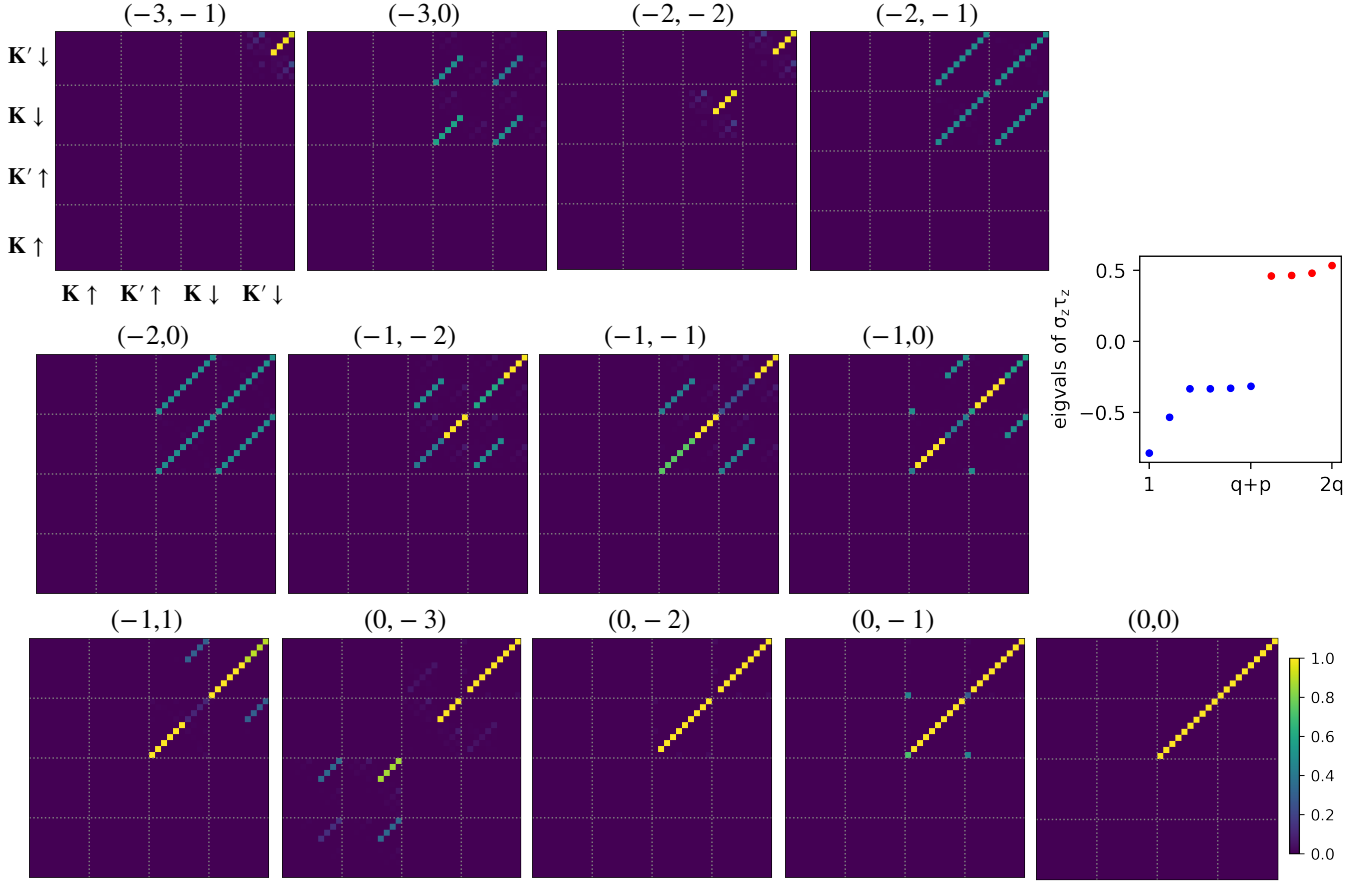


FIG. S19. Absolute values of the full density matrices at $\mathbf{k} = \mathbf{0}$ for all main gapped states at 1.05° and $\phi/\phi_0 = 1/5$ in absence of heterostrain, expressed in the eigenbasis of the $\sigma_z \tau_z$ operator. At a general flux ratio $\phi/\phi_0 = p/q$, the eigenstates of $\sigma_z \tau_z$ split into $q + p$ (blue) and $q - p$ (red) groups separated by a spectral gap, and are descendants of the zero field $+1$ and -1 Chern bands respectively. Near the magic angle, Coulomb interaction and magnetic field favor correlated gapped states that do not couple opposite Chern bands.

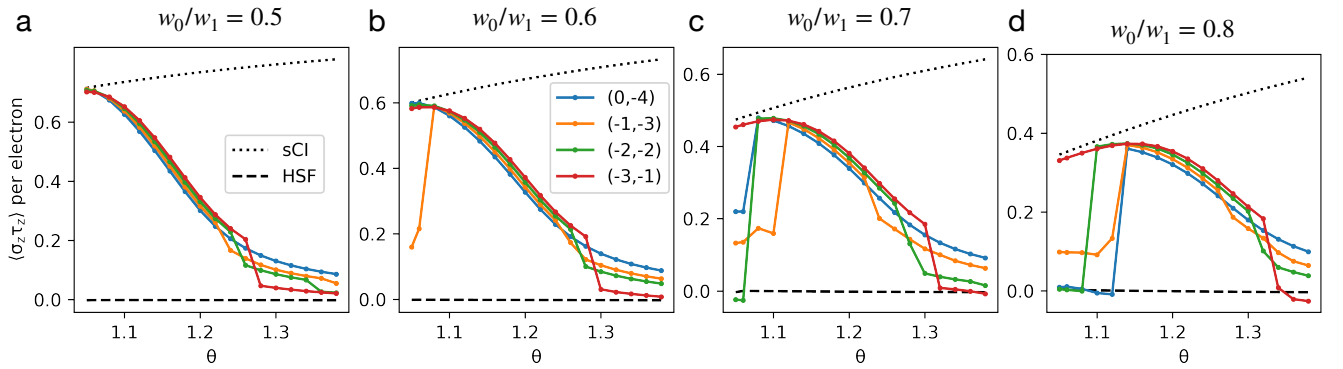


FIG. S20. Averaged $\langle \sigma_z \tau_z \rangle$ for the occupied electronic states at ϕ/ϕ_0 , twist angle $\theta = 1.05^\circ$ in the absence of heterostrain, for different ratios of w_0/w_1 . As w_0/w_1 is decreased, the correlated Hofstadter ferromagnets persist toward lower angles, before losing to other gapped states with intervalley coherence. The phase transition is first order, and marked by a collapse of $\langle \sigma_z \tau_z \rangle$.